International Journal of Solids and Structures 306 (2025) 113072

Contents lists available at ScienceDirect

International Journal of Solids and Structures

journal homepage: www.elsevier.com/locate/ijsolstr

Two-way coupled modeling of dislocation substructure sensitive crystal plasticity and hydrogen diffusion at the crack tip of FCC single crystals

Tang Gu [a,b,*], Baolin Wang [a], Ting Zhu [a,c], Gustavo M. Castelluccio [d], David L. McDowell [a,c]

[a] Woodruff School of Mechanical Engineering, Georgia Institute of Technology, Atlanta, GA 30332, USA
[b] DR2I, Institute of Polytechnic Science and Aeronautics (IPSA), 94200 Ivry-Sur-Seine, France
[c] School of Materials Science and Engineering, Georgia Institute of Technology, Atlanta, GA 30332, USA
[d] School of Aerospace, Transport and Manufacturing, Cranfield University, Bedfordshire MK43 0AL, UK

ARTICLE INFO

Keywords:
Hydrogen transport
Crystal plasticity
Finite element modeling
FCC crystals
Hydrogen effects on crack tip fields
Coupled chemomechanical effects

ABSTRACT

Dislocation substructure-sensitive crystal plasticity (DSS-CP) modeling accounts for the evolution of mesoscale structures using dislocation-based parameters informed by experiments and computation at various lower length scales. To a first-order approximation, DSS-CP model parameters are affected by hydrogen (H) concentration, accounting for both H-dependent yield strength and strain hardening rate. This H-affected DSS-CP model is two-way coupled with H-diffusion to explore both effects of plastic deformation on H-diffusion and effects of H on yield strength and strain hardening in the DSS-CP model. Crack tip simulations are performed for face-centered cubic (FCC) metals under monotonic loading conditions with and without H. Enhanced maximum plastic deformation in the vicinity of the crack tip (i.e., localization or intensification of plastic strain) and crack tip opening displacement (CTOD) are predicted in the presence of H, consistent with experimental observations. In spite of increased initial strength due to H, subsequent reduction of the rate of strain hardening in the presence of H is shown to enhance localization of crack tip plasticity. Furthermore, this modeling framework predicts that higher H-diffusivity (leading to a larger H-affected zone) will enhance the crack tip plasticity, making use of the two-way coupling algorithm implemented in this work. On the other hand, we find that the H-sensitivity of crack tip strain localization response, based only on modification of model parameters, is too weak to explain typical experimental observations. This points to the need to develop more advanced DSS-CP constitutive relations that consider highly complex dislocation interactions with point defects.

1. Introduction

Metals play a critical role in such diverse structural applications as sustainable energy, transportation, healthcare, infrastructure, and public safety, owing to their excellent load bearing capacity, ductility, and damage tolerance. Under a hydrogen (H) environment, H embrittlement (HE) of face-centered cubic (FCC) alloys is manifested as a reduction of tensile ductility in monotonic loading tests (Abraham and Altstetter, 1995; Feng et al., 2022; Han et al., 1998; Li et al., 2023b), and by the acceleration of the fatigue crack growth rate under cyclic loading (Murakami et al., 2008; Schuster and Altstetter, 1983; Wang et al., 2018). Although HE is a longstanding technological challenge to structural applications (Fekete et al., 2018), its microscopic mechanisms are still unsettled and this continues to be an active area of research. Significant intensification or localization of plastic deformation and associated slip banding have been observed at high H concentrations, based on transmission electron microscopy (TEM), electron backscatter diffraction (EBSD) and atomic force microscopy (AFM) observations (Aubert et al., 2010; Hatano et al., 2014). In addition, smaller dislocation cells and dense dislocation walls are observed near notches or crack tips, compared to coarser dislocation cell structures in the absence of H (Wang et al., 2017; Wang et al., 2018). Supported by *in situ* TEM and EBSD, the H-enhanced localized plasticity (HELP) mechanism has been proposed (Robertson et al., 2015), suggesting that H enhances plastic deformation and accelerates the evolution of dislocation substructure. In addition to H-enhanced strain localization, prior works have also considered that H influences material damage by reducing ductility via particle decohesion, vacancy stabilization, void coalescence or formation of hydrides (Luo et al., 2017; Neeraj et al., 2012; Tehranchi et al., 2020; Xie et al., 2016).

* Corresponding author.
E-mail address: tang.gu@me.gatech.edu (T. Gu).

https://doi.org/10.1016/j.ijsolstr.2024.113072
Received 7 December 2023; Received in revised form 2 August 2024; Accepted 7 September 2024
Available online 19 September 2024

Monotonic and cyclic fatigue mechanical tests have been conducted for smooth specimens precharged with H. (Abraham and Altstetter, 1995) reported stress–strain curves for polycrystalline FCC 310 stainless steel (SS) under monotonic loading at various levels of H concentration. Their results demonstrated that higher H concentration leads to increased yield strength. In addition, a reduction of the strain hardening rate with H is observed at very high levels of H concentration. Furthermore, (Hachet et al., 2021; Hachet et al., 2020) investigated the competition between H-induced softening and hardening effects on cyclic behavior for FCC nickel (Ni) single crystals, revealing complex interactions with dislocation organization, vacancies, and vacancy clusters that influence long-range internal stresses and material behavior. To investigate H-induced reduction of ductility, H-accelerated fracture/crack propagation, and HE mechanisms, a series of mechanical models accounting for H effects have been developed. For instance, a H-affected phase field approach (Martínez-Pañeda et al., 2018), damage models (Depraetere et al., 2021; Li et al., 2023a; Ogosi et al., 2020), and cohesive zone models (Gobbi et al., 2019) account for either strong or weak coupling effects with varying H concentrations.

To incorporate H effects into the study of crystal deformation, several H-affected crystal plasticity (CP) models have been developed (Schebler, 2011; Vasios, 2015). Recently, a dislocation substructure sensitive crystal plasticity (DSS-CP) model for FCC crystals has been recently developed (Castelluccio and McDowell, 2017), and extended to directly incorporate effects of H on model parameters in a physically-plausible way (Castelluccio et al., 2018). This DSS-CP model accounts for evolution of mesoscale dislocation substructures at appropriate lower length scales informed via experiments, theory, and computation. Note that it does not explicitly consider point defect concentrations, but rather assumes that dislocation line tension, thermal stress and activation energy depend on H. It was demonstrated that the model responses were consistent with key experimental trends regarding the influence of H on stress–strain behavior of FCC crystals, assuming prescribed levels of uniform H concentration that would typically be associated with precharging. Additionally, a dislocation density based CP model (Yuan et al., 2020) has been developed to account for H effects on the dislocation line energy, while assuming a uniform H concentration in FCC polycrystals. While many experiments to date have considered specimens precharged with H, in actual applications flux of H is introduced at the crack tip from crack faces exposed to environmental reactions (Neeraj et al., 2012; Saintier et al., 2011). Therefore, the physical understanding of H distribution and its effects on inelastic crack tip fields is much more complex than that of a uniform H distribution, particularly when considering material models decoupled from H transport. In this context, (Singh et al., 2022) has explored the two-way coupling between H distribution within polycrystals and H-affected mechanical behavior.

For a comprehensive understanding of H distribution and its effects on HE, it is essential to couple mechanical deformation with H transport models. Early works coupled a H-transport model with a phenomenological J_2 plasticity model framework for polycrystals to simulate crack tip fields (Krom et al., 1999; Sofronis and McMeeking, 1989). The framework for transport of H considers that atomic H resides both in normal interstitial lattice sites (NILS) (i.e., lattice concentration of H) and in trapping sites at defects (e.g., dislocation cores, vacancies, grain boundaries). In this H transport model, trapping of H is enhanced by plastic deformation, and H diffusion through the lattice is affected by the hydrostatic stress gradient. Subsequently, the CP models have been coupled with a variety of H transport models to evaluate H distribution within single crystals/polycrystals, e.g., (Charles et al., 2017; Ilin et al., 2014; Kumar and Mahajan, 2020). In the majority of these studies, there is an assumption that CP model parameters remain unaffected by fluctuations in H concentration.

Coupling of H transport with inelastic deformation involves two companion processes: (i) plastic deformation enhances H transport and (ii) H influences material yielding and strain hardening rates. Although not the focus here, there are significant prior hypotheses regarding the effects of H on material inelastic strain response; a prominent example is the HELP mechanism (Robertson et al., 2015). Our intent is to simulate the nature of these coupled processes near a blunted crack tip in terms of their influence on the crack tip strain field. This study is motivated by a lack of attention devoted to computational studies of two-way coupled simulation of crack tip H transport and dislocation plasticity for single crystals, and in particular a lack of systematic consideration of the relative influence of H on localization of the crack tip strain field due to enhancement of yield strength and reduction of the strain hardening rate. With such simulations we can explore the sensitivity of H effects on model parameters with the crack tip field strain localization.

To this end, we employ a dislocation density-based CP framework (i.e., DSS-CP) with incorporation of H influence on certain parameters for FCC metals (Castelluccio et al., 2018) in the context of full two-way coupling with H transport to study crack tip strain localization in the presence of H. Moreover, dependence of the DSS-CP model parameters on H-concentration will be considered in terms of their influence on crack tip strain localization. In particular, we conduct a DSS-CP parameter sensitivity study to explore whether the effect of yield strength or rate of strain hardening dominates crack tip strain localization. We do not consider reduction of ductility or fracture resistance (Neeraj et al., 2012) in this work, instead focusing on the issue of crack tip strain localization at a blunted crack tip. Such enhancement of plastic strain localization is generally observed as a precursor or companion to HE processes (Robertson et al., 2015; Sun et al., 1995).

The outline of the article is as follows. H-affected DSS-CP and H transport models are presented in Section 2. Section 3 pursues computational simulation of H effects near a blunted crack tip, via a two-way coupling algorithm accounting for the H transport/microstructural deformation interactions. Section 4 presents simulation results, including the distribution of H concentration, crack tip plastic strain fields with and without H, and the H-affected crack tip opening displacement (CTOD). Finally, Section 5 investigates the roles of H-reduced strain hardening rate, H-enhanced yield strength, and H-diffusivity in promoting crack tip plasticity, as well as a comparison between the assumption of homogenous H-distribution versus the two-way chemo-mechanical coupling algorithm.

2. H-affected DSS-CP model and two-way coupling with H transport

CP theory involves constitutive laws governing slip and hardening on individual slip systems, encompassing relations between resolved shear stress and plastic shearing rate on various slip systems. The integration of CP theory and finite element analysis gives rise to the Crystal Plasticity Finite Element Method (CPFEM), facilitating microstructure-scale simulations of mechanical behavior in crystalline materials. CPFEM plays a crucial role in investigating interactions involving crystallographic texture, grain characteristics, and orientation and misorientation distributions within polycrystalline structures, e.g., (Gu et al., 2017; Gu et al., 2019). CP constitutive laws for single crystals have increasingly focused on physically-based approaches that are less phenomenological and incorporate information from multiple scales. (Castelluccio and McDowell, 2017) considered the mesoscale evolution of dislocation substructures during cyclic loading and developed a DSS-CP model for FCC single crystals with 12 slip systems. This DSS-CP model has the following key features:

- Physically-based formulations of threshold and back stresses, allowing the model to address cyclic loading conditions and the influence of dislocation cell structures.
- Evolution of mobile screw dislocation density on each slip system.
- Dislocation substructures are assumed to exist as observed by TEM under loading with various strain amplitudes and strain states.
- Various physical phenomena at lower length scales are incorporated, and the related material parameters can be estimated by TEM

observations or informed by other models, including unit process models, atomistic simulations and dislocation dynamics.
- First order effects of H on physical mechanisms and associated material parameters are considered (Castelluccio et al., 2018), i.e., reduced stress required to bow out a dislocation owing to a H-induced reduction in the line energy of edge dislocations.

The DSS-CP model was previously implemented in a user material subroutine (UMAT) in the ABAQUS finite element (FE) code (Smith, 2009). Simulations were carried out for both single crystals and polycrystals. The simulation results regarding cyclic stress–strain behavior were obtained for various FCC materials, such as Ni, Cu, and 316L SS. In these simulations, the model parameters were first determined based on literature data, TEM observations and atomistic simulation results, and then slightly adjusted to better fit the experimental measured stress–strain behaviors (Castelluccio and McDowell, 2017).

The H-affected DSS-CP constitutive laws for FCC metals and alloys are summarized as follows. Interested readers are referred to (Castelluccio and McDowell, 2017) for a more comprehensive presentation of the constitutive equations. The thermally activated shearing rate for slip system $\alpha(=1,\ldots,12)$ is given by

$$\dot{\gamma}^{\alpha} = \rho_m^s \bar{l} b \nu_G \exp\left(-\frac{\Delta G\left(\tau_{eff}^{\alpha}\right)}{k_B T} \right) \mathrm{sgn}(\tau^{\alpha} - B^{\alpha}) \tag{1}$$

where ρ_m^s is the density of mobile (screw) dislocations, $\bar{l}$ is the mean advance distance of a dislocation in between obstacle bypass events, b is the Burgers vector length $\sim 2.5^{-10}$ m, τ^{α} is the local slip system resolved shear stress, and ν_G is the attempt frequency $\sim 10^{12}$ s^{-1}. Here, ΔG is the activation enthalpy required to bypass short range obstacles, τ_{eff}^{α} is the effective stress, k_B is the directional intragranular slip system back stress, k_B is the Boltzmann constant (8.617 eV·K^{-1}), and T is the absolute temperature.

The form of ΔG pertaining to the mean dislocation barrier has been parameterized as (Kocks and Mecking, 2003)

$$\Delta G\left(\tau_{eff}^{\alpha}\right) = F_0 \left(1 - \left[\frac{\tau_{eff}^{\alpha}}{s_t^{0}\frac{\mu}{\mu_0}} \right]^{p} \right)^{q} \tag{2}$$

where F_0 is the activation energy for thermally activated barrier bypass of dislocations at $\tau_{eff}^{\alpha} = 0$ MPa, p and q are profiling parameters of the nonlinear relation of ΔG versus τ_{eff}^{α}, and s_t^0 is thermal slip resistance at 0 K. In addition, μ and μ_0 represent the shear modulus (C_{44}) at temperature T and 0 K, respectively. The effective stress that drives the barrier bypass at the slip system level is defined by

$$\tau_{eff}^{\alpha} = \langle |\tau^{\alpha} - B^{\alpha}| - S^{\alpha} \rangle. \tag{3}$$

Here, S^{α} is the nondirectional threshold stress. The Macauley bracket is defined for argument g by $\langle g \rangle = 0$, if $g \leq 0$, $\langle g \rangle = g$ if $g > 0$. The threshold stress required to bow a dislocation against a dislocation pile-up between dislocation walls is given by

$$S^{\alpha} = S_0^{\alpha} + \alpha_{LE} \frac{\mu b}{(1 - f_w) d_{struct}} + \mu b \left(A_{ii} \rho^{\alpha} \right)^{1/2} \tag{4}$$

where S_0^{α} corresponds to an intrinsic resistance. The second term in equation (4) corresponds to the stress required to bow-out a dislocation and depends on the dislocation line energy α_{LE} and dislocation wall volume fraction f_w. The third term corresponds to the interaction between collinear dislocations in pile-ups and is mediated by the self-interaction coefficient, A_{ii}. In its present form (Castelluccio et al., 2018), the model assumes that H couples with the material model via a specific set of parameters. These H-dependent DSS-CP parameters will be discussed in Section 3.2, including the activation energy F_0, thermal slip resistance s_t^0, and line tension coefficient α_{LE}; F_0 and s_t^0 account for H-enhanced yield strength, while α_{LE} accounts for effects of H on the rate of strain hardening. In the spirit of the earlier work of (Castelluccio et al., 2018), no attempt is otherwise made in the present work to explicitly couple the material behavior with point defects, or to describe H-enhanced failure processes.

In previous studies (Krom et al., 1999; Sofronis and McMeeking, 1989), an H transport model was developed and coupled with macroscopic phenomenological J_2 plasticity models to facilitate crack tip FE simulations. H concentrations in the lattice and traps (denoted by C_L and C_T, respectively) are considered by these models and depend on the effective plastic strain and hydrostatic stress gradient. Specifically, the trap density N_T is coupled with the effective plastic strain for BCC metals (Krom et al., 1999; Sofronis and McMeeking, 1989) and coupled with the total dislocation density ρ_{tot} for FCC crystals (Dadfarnia et al., 2015). Additionally, N_T is proportional to C_T, which maintains local equilibrium with C_L. In this work, we extend this H transport approach in conjunction with DSS-CP to model crack tip fields in a single crystal. Considering that heat transfer and mass diffusion equations have the same form, the H transport simulation is performed by writing a user subroutine UMATHT in ABAQUS as a proxy. As such, the C_L field is analogous to the temperature field and can be tracked in ABAQUS simulations (Oh et al., 2010).

Following the H transport model by (Sofronis and McMeeking, 1989), H is considered to move through the material via migration along NILS. Transported H resides either at NILS or trapping sites related to crystal defects. NILS and trapped H populations are in equilibrium according to Oriani's theory (Oriani, 1970), i.e.,

$$\frac{\theta_T}{1 - \theta_T} = \frac{K \theta_L}{1 - \theta_L} \tag{5}$$

where θ_L is the NILS occupancy (i.e., the ratio of the occupied NILS to the total available sites), and θ_T is the trapping site occupancy. The parameter K represents equilibrium partitioning between NILS and trapping sites, i.e.,

$$K = \exp\left(\frac{W_B}{RT} \right) \tag{6}$$

where the trap binding energy W_B is taken as 10 kJ/mol for FCC crystals (Thomas, 1980), and the universal gas constant $R = 8.314$ J/(mol K). Additionally, the material parameters for the H transport model are summarized in Appendix C. The NILS H concentration, C_L, measured in H atoms per unit volume (atoms/m^3), can be expressed as

$$C_L = \theta_L \beta_H N_L \tag{7}$$

where β_H denotes the number of NILS per solvent atom and N_L denotes the number of solvent atoms per unit volume (atoms/m^3), given by

$$N_L = N_A / V_M \tag{8}$$

Recall that $N_A = 6.023 \times 10^{23}$ (atoms/mol) is Avogadro's number, and $V_M = 7.11 \times 10^{-6}$ is the molar volume of the host lattice measured in the unit of volume per mole (m^3/mol) (Boyer and Gall, 1985; Dadfarnia et al., 2015). Similarly, the H concentration at traps, C_T, measured in H atoms per unit volume, can be written as

$$C_T = \theta_T \alpha_H N_T \tag{9}$$

where α_H denotes the number of H atom sites per trap, and N_T denotes the number of traps per unit lattice volume. Taking into account the assumption of one trap per atomic plane associated with a dislocation line (Tien et al., 1976), the dislocation trap density N_T is expressed in relation to the total dislocation density ρ_{tot} as

$$N_T = \frac{\lambda \rho_{tot}}{a_{lattice}} = \frac{\lambda \eta_m \sum \rho_m^{s\alpha}}{a_{lattice}} \tag{10}$$

where $a_{lattice}$ (0.358 nm) is the lattice parameter and $\lambda = \sqrt{3}$ for FCC metals (Dadfarnia et al., 2015); the total dislocation density ρ_{tot} is estimated based on the sum of the mobile dislocation density $\rho_m^{s\alpha}$ on each slip system obtained from the DSS-CP model; η_m denotes the ratio between ρ_{tot} and $\sum \rho_m^{s\alpha}$. Under H-charging, ρ_{tot} is observed to be approximately 1.33 times larger than $\sum \rho_m^{s\alpha}$ for single crystal FCC Ni (Hachet et al., 2020), leading to the establishment of η_m as 1.33.

Through equations (5), (7), and (9), together with the assumption $\theta_L \ll 1$ (Oriani, 1970), the H concentration at trapping sites C_T is related to the lattice concentration C_L according to

$$C_T = \frac{K \frac{\alpha_H N_T}{\beta_H N_L} C_L}{1 + \frac{K}{\beta_H N_L} C_L} \tag{11}$$

The governing equation for transient H-diffusion accounting for trapping and hydrostatic drift are given by (Sofronis and McMeeking, 1989)

$$\frac{D}{D_{eff}} \frac{\partial C_L}{\partial t} - \nabla \cdot (D \nabla C_L) + \nabla \cdot \left(\frac{D C_L \overline{V}_H}{RT} \nabla \sigma_H \right) = 0 \tag{12}$$

where $\partial / \partial t$ is the local time derivative, ∇ is the gradient operator, $(\cdot)$ denotes the divergence, D is the H-diffusivity, and the effective H diffusivity D_{eff} is expressed as

$$D_{eff} = D \frac{C_L}{C_L + C_T (1 - \theta_T)} \tag{13}$$

Additionally, σ_H is the hydrostatic stress, i.e., $\sigma_H = \frac{1}{3} \sum_{i=1}^{3} \sigma_{ii}$, and $\overline{V}_H$ is the partial molar volume of H in solid solution, i.e., 2×10^{-6} (m^3/mol) for FCC metals (Dadfarnia et al., 2015; Moody et al., 1990).

In this work, we adopt the H-diffusion model by (Sofronis and McMeeking, 1989). The "strain rate" effect on H-diffusion is considered negligible based on earlier studies (Krom et al., 1999). It has been noted that the strain rate effect can lower the H concentration in lattice sites due to the filling of trap sites. However, given the relatively low load and short H charging time compared to the literature (see detailed discussion in Section 3.1), our simulations are conducted under quasi-static loading conditions (with strain rates near the crack tip around 10^{-3} s^{-1}), providing rather short times for H to enter traps. Therefore, the impact of the strain rate effect on H concentration is deemed less significant in our study.

Furthermore, the primary goal of this work is to model H-enhanced crack tip plasticity and CTOD by combining a widely used H transport model (Sofronis and McMeeking, 1989) and a recently developed DSS-CP model (Castelluccio et al., 2018). It is found the H transport model (Sofronis and McMeeking, 1989), without consideration of the strain rate effect, is sufficient to achieve the goal (see Section 4).

3. Computational simulation of H effects near a blunted crack tip

3.1. Crack tip simulation

To study the interactions between H transport and crack tip plastic deformation, blunted crack tip simulations are pursued in this work. Experimental observations of cracks in H-affected materials motivate consideration of a blunted rather than sharp crack tip. As illustrated in Fig. 1, the simulated crack lies in the (010) plane and the crack front lies along the $[\bar{1}01]$ direction. For this specific crystal orientation and type of loading used in the crack tip simulation for an FCC single crystal, only three conjugate-pair slip systems (i.e., $(1\bar{1}1)[110]$ & $(1\bar{1}1)[011]$; $(\bar{1}11)[101]$ & $(11\bar{1})[101]$; and $(111)[1\bar{1}0]$ & $(111)[01\bar{1}]$ are active (Patil et al., 2008b; Rice, 1987). The other slip systems are inactive. By virtue of symmetry of both elastic and plastic anisotropies, an in-plane cross section of the finite element mesh, with a single element through the thickness, is used in this work for crack tip simulation. This cross section has a half disk containing a notched crack, and its outer boundary is imposed with displacements from a plane-strain crack tip field with Mode I stress intensity factor K_I (Patil et al., 2008b). Symmetry boundary conditions are applied along the crack extension line (i.e., $u_2 = 0$ along $x_2 = 0$).

The notch radius r and the outer radius R of the simulation domain are 5 μm and 5 mm, respectively. The notch root is spanned circumferentially by 10 elements. The element size near the notch root is about 1 μm, indicative of the minimum domain size for averaging the deformation substructure. The ABAQUS element type C3D20RT is used (Smith, 2009), i.e., 20-node thermally coupled quadratic brick with reduced integration (2×2×2 integration points) and hourglass control. The reduced integration elements are selected for three main reasons: (i) They are better suited for severe plastic deformation, such as crack tip simulations, as full integration elements tend to be too stiff and unsuitable for such analyses. (ii) They help to reduce computational time in the DSS-CP models, thereby avoiding excessively long simulations. (iii) This element type allows the hydrostatic stress gradient $\nabla \sigma_H$ to be calculated within each element, facilitating numerical implementation (see Section 3.4).

As previously mentioned, symmetry conditions are imposed ahead of the crack front since the particular configuration selected is one of crystallographic symmetry relative to the crack orientation (Patil et al., 2008a; Patil et al., 2008b). Such symmetry is not generally applicable to arbitrary crack orientations in single crystals. This configuration promotes multislip ahead of the crack tip, consistent with long crack

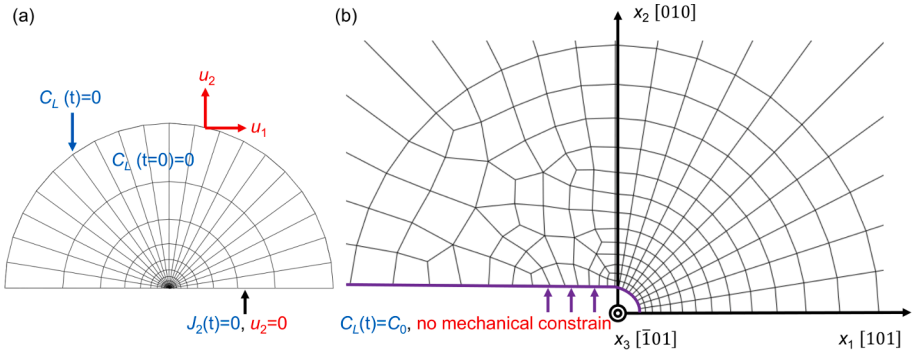

Fig. 1. Semi-circular domain containing a blunted crack in a single grain: (a) Finite element mesh; (b) Detailed view of the near-tip region. Initial and boundary conditions for the coupled DSS-CP and H transport problem are given; u_1 and u_2 are the asymptotic displacements in x_1- and x_2-directions, respectively. Parameter C_0 is the NILS H concentration at the crack faces. Displacement u_2 and normal H flux J_2 are both zero along the crack extension line due to symmetry conditions. The crack lies on the (010) plane of FCC crystal lattice, with the crack front along the $[\bar{1}01]$ direction.

scenarios (Cuitino and Ortiz, 1993; Patil et al., 2008b) subjected to Mode I loading. The plane-strain Mode I crack tip K-field prescribed as the displacement boundary condition at the exterior boundary of the circular domain is based on the isotropic elastic solution, assuming small-scale plasticity at the crack tip (Bichon et al., 2008; Saeedvafa and Rice, 1989), i.e.,

$$u_i = \frac{K_I}{2G}\sqrt{\frac{R}{2\pi}} f_i(\theta) \tag{14}$$

Here, u_i ($i = 1, 2$) is the displacement field, K_I is the stress intensity factor, (R, θ) are the polar coordinates with the origin at the crack tip, and f_i is the angular distribution function given by

$$\begin{aligned} f_1 &= \cos\left(\frac{\theta}{2}\right)\left[\kappa - 1 + 2\sin^2\left(\frac{\theta}{2}\right)\right] \\ f_2 &= \sin\left(\frac{\theta}{2}\right)\left[\kappa - 1 + 2\sin^2\left(\frac{\theta}{2}\right)\right] \end{aligned} \tag{15}$$

where $\kappa = 3 - 4\nu$ for plane strain, ν is Poisson's ratio, and G is the isotropic elastic shear modulus. The displacement boundary condition is implemented in ABAQUS via a user subroutine DISP. In our crack tip simulations under monotonic loading, the maximum value of K_I is 10 MPa$\sqrt{\text{m}}$, applied at a constant rate over a rise time of 51 s, which is consistent with experiments employed for comparison. The aim is to compare the DSS-CP model responses with the experimental observations of H-affected slip band forming near the crack tip of single crystal Ni in the further work. Although the use of an isotropic K field in Eq. (14) does not accord with the anisotropic elastic solution for this single crystal, it adequately serves the purpose of serving as a remote loading condition.

Boundary conditions for the H transport problem are presented in Fig. 1. The crack surface is set to maintain a constant NILS H concentration C_0, which corresponds to the H concentration prescribed at the crack faces in equilibrium with environmental H_2 at a pressure of 1 atm for FCC metals; C_0 is taken as 7.996×10^{24} H atoms/m^3 (9.44×10^{-5}H atoms per solvent atom) (Dadfarnia et al., 2015). In this study, the H-affected DSS-CP model parameters are considered to depend on the normalized H concentration C_L/C_0. Note that the distribution of C_L/C_0 ahead of the crack tip is not influenced by the absolute value of C_0, in contrast to parameters such as H diffusivity D, trap density N_T and the hydrostatic stress gradient $\nabla\sigma_H$ in the H transport model. We assume H-diffusivity $D = 5 \times 10^{-13}$ m^2/s based on the experimental data for Ni at the room temperature (Völkl and Alefeld, 1978). Furthermore, various coefficients of H-diffusivity will be explored in Section 5.3. In Equations (14) and (15), ν and G are assigned values of 0.31 and 78 GPa, respectively, for polycrystalline Ni (for remote loading condition).

3.2. H-affected mechanical behavior and model parameters

In previous work (Castelluccio and McDowell, 2017), the DSS-CP parameters were assigned to match the stress–strain curves of FCC Ni at room temperature in the absence of H (see Appendix C). Based on previous experimental studies, e.g., (Abraham and Altstetter, 1995; Ghermaoui et al., 2019; Yagodzinskyy et al., 2009), H has substantial effects on the mechanical properties of FCC metals (see Fig. 2(a)). To account for H effects on mechanical responses for common FCC metals, we follow the earlier work (Castelluccio et al., 2018) and consider the direct effects of H on dislocation slip resistance. The limits or bounds of mechanical behaviors for Ni single crystals loaded in uniaxial tension along the [010] direction without and with a high uniform concentration of H are plotted in Fig. 2(b).

It is worth noting that the DSS-CP model focuses on the H-effect on the constitutive law of common FCC single crystals (e.g., Ni, austenitic stainless steel, etc.). Therefore, the H-affected stress–strain curves by the experiments of (Abraham and Altstetter, 1995) for 310 SS (i.e., stainless steel with a high content of Ni) are used here for parameter identification, as a considerably high H concentration (i.e., near saturation) has been charged in the specimens. We assume that the strong H-affected mechanical behavior corresponds to the behavior at the notch root.

Our collaborators performed atomistic simulations of screw obstacle-cutting using an in-house free-end nudged elastic band (FENEB) code (Zhu et al., 2007) with an embedded atom method (EAM) potential of Ni (Angelo et al., 1995; Baskes et al., 1997). Detailed simulations are referred to their previous paper (Chen et al., 2019). The activation energy (i.e., F_0) for obstacle-cutting as a function of resolved shear stress (s_t^0) for different types of obstacles, i.e. Vacancy (Va), Va-1H and Va-6H complex, have been investigated. It is seen that the activation energy of obstacle-cutting increases with the amount of H atoms inside the vacancy. This result confirms that the H-Va complexes are strong pinning obstacles to dislocation glide for FCC metals. These works are currently in preparation for publication. Moreover, based on in-situ TEM observations performed by (Xie et al., 2016), experiments conducted on FCC Al pillars in the presence of H show that the flow stress more than

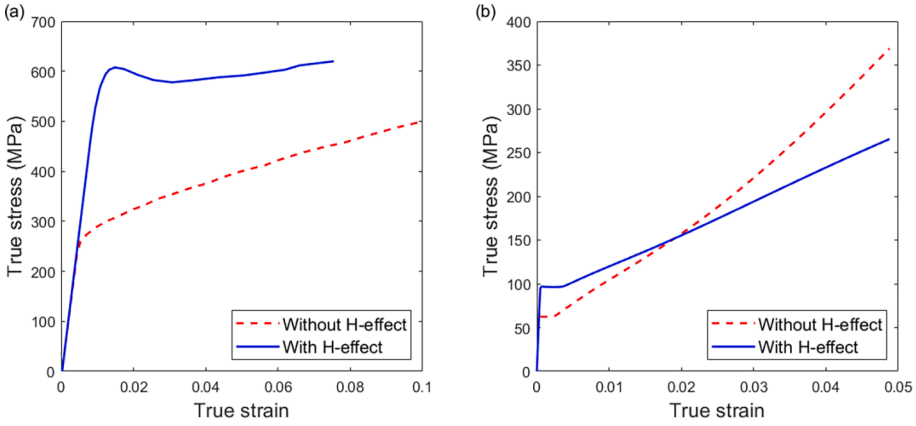

Fig. 2. (a) Experimental stress–strain curves for polycrystalline FCC 310 SS without and with H charged (Abraham and Altstetter, 1995). The experiments demonstrate that with a near-saturated high H concentration, the yield strength is doubled, while the strain hardening rate is reduced by half for common FCC metals. (b) Bounds on H effects on uniaxial tensile true stress–strain curves simulated by the H-dependent DSS-CP model (Castelluccio et al., 2018) for Ni single crystals loaded along the [010] direction at a strain rate of 10^{-3} s^{-1} at room temperature. Refer to Appendix C for calibration of the DSS-CP parameters without H. Model responses with extremely high uniform H concentration (i.e., $C_L/C_0 = 1$) and without H are compared. The activation energy F_0 and thermal slip resistance s_t^0 depend on H concentration, accounting for H-doubled yield strength. Simultaneously, the line tension coefficient α_{LE} accounts for the reduced strain hardening rate by half with H.

doubles. This observed additional resistance to deformation has been attributed to superabundant hydrogenated Va.

While atomistic simulations and in-situ TEM observations have demonstrated that the presence of H leads to an increase in F_0 and s_t^0, quantifying model parameters is still challenging. The difficulty lies in quantitatively analyzing parameters when transitioning across different scales of models. For example, the parameter changes obtained from atomistic simulations represent values only under specific microstructures and cannot be directly applied to the DSS-CP model. Hence, we choose to adjust the parameters of the H-dependent DSS-CP model using existing H-affected experimental stress–strain curves. To reproduce the doubled enhancement of yield strength at considerably high H concentrations as observed by (Abraham and Altstetter, 1995) (see also Fig. 2 (a)), we increase F_0 and s_t^0 by 20% at these high levels of H.

On the other hand, in terms of multiscale modeling, there is no consensus regarding the role of H on the rate of strain hardening; as a simple placeholder for this effect, we assume that the H-induced reduction of the rate of strain hardening rate is attributed to the reduction of line tension. In particular, following (Castelluccio et al., 2018; Yu et al., 2020), we assume that H can reduce the stress to bow out a dislocation due to the H-induced decrease of line tension of an edge dislocation. As illustrated in Fig. 2(a), experimental stress–strain curves for FCC 310 SS (Abraham and Altstetter, 1995) demonstrated that the strain hardening rate reduces by a factor of two at high H concentrations. In the present work, a 50 % reduction in the line tension coefficient α_{LE} is assumed at high H, i.e., 0.5 versus 1.0 with/without H, respectively. This alteration leads to a substantial decrease by a factor of two in the strain hardening rate with H relative to its absence. As illustrated in Fig. 2(b), the model response at high H levels (C_L/C_0=1) is compared to that without high uniform H.

A similar trend of H-effect has been observed for FCC single crystal Ni (Ghermaoui et al., 2019; Yagodzinskyy et al., 2009), but with a less pronounced reduction in the strain hardening rate. We preliminarily calibrated the DSS-CP model parameters to reproduce these experimental data and observed a minimal influence of H on crack tip plasticity. This discrepancy with the observed enhancement of crack-tip deformation with H (see Appendix A) suggests that these experimental stress–strain curves may not fully represent the mechanical behavior at the crack tip. We deem that factors such as H concentration and material deformation state discussed in these references may not be relevant to crack-tip simulation. Additionally, a systematic parametric study will be conducted for the H-affected parameters (i.e., α_{LE}, F_0, and s_t^0) in Section 5 to investigate their roles in enhancing crack tip plasticity. It is found that as the variations in H-affected DSS-CP model parameters decrease, the significance of H-enhanced crack tip plasticity diminishes. This study elucidates that ensuring significant H-induced effects on the DSS-CP model parameters reproduces H-enhanced crack tip plasticity.

3.3. Variation of DSS-CP parameters with respect to H-concentration

Pursuit of H-coupled simulations of crack tip fields requires assignment of the direct dependence of DSS-CP parameters (α_{LE}, F_0, and s_t^0) on intermediate values of H-concentration that evolve in connection to each initial-boundary value problem for coupled H diffusion and mechanical fields. To this end, we assume a sigmoidal interpolation between normalized H concentration in lattices C_L/C_0 and the associated mechanical parameters. This constitutes a first order assumption that the DSS-CP parameters depend on the C_L, neglecting effects of H concentration in traps C_T or the sum $C_{tot} = C_L + C_T$. We make this assumption for two reasons: (i) using the boundary conditions and modeling parameters employed in this work, C_T/C_0 values computed by the DSS-CP model are much smaller than C_L/C_0 values (see Section 4.1), leading to a negligible influence of C_T compared to C_L; (ii) the mechanisms by which H affects the DSS-CP mechanical parameters are not fully clear at crystal scale, e.g., it is still unsettled whether the "dislocation line tension" mechanism is physically associated with C_L, C_T, or C_{tot}. Our research collaborators are carrying out atomistic simulations and dislocation dynamics simulations at lower scales for further investigations, e.g., (Lin et al., 2021a; Lin et al., 2021b), including recent parallel advances that incorporate H trapping at vacancies with pronounced effects on crack tip distribution of H (Zirkle et al., 2021a) as well as dislocation mobility, strain softening and progression of failure processes via bypass of vacancy clusters and coalescence of vacancies (Zirkle et al., 2023). The intent of the current work is to explore the extent to which direct dependence of DSS-CP parameters can contribute to these effects.

Abraham and Altstetter (Abraham and Altstetter, 1995) introduced an extremely high H concentration as large as 9.2 atomic percent. Also, they suggested second phases (e.g., hydrides) will be possibly produced if charged at higher H concentration. Hence, we assume $C_{\text{saturation}} = 9.2$ atomic percent. As illustrated in Fig. 3(a), H-enhanced yield strength σ_Y is plotted in terms of various normalized H concentration, i.e., $C_{\text{normalized}} = C/C_{\text{saturation}}$, for FCC 310 SS, where C indicates various H concentration charged in (Abraham and Altstetter, 1995). In this work, a sigmoidal interpolation is adopted, i.e.,

$$\sigma_Y(C_{Normalized}) = \frac{(\sigma_Y)_{\max} - (\sigma_Y)_{\min}}{1 + \exp\left[-a_{interp}\left(C_{Normalized} - b_{interp}\right)\right]} + (\sigma_Y)_{\min} \tag{16}$$

where $(\sigma_Y)_{\max} = 610$ MPa and $(\sigma_Y)_{\min} = 270$ MPa, respectively. In addition, $a_{interp} = 10.0$ and $b_{interp} = 0.38$ are set as profile parameters. Without further guidance, we tacitly assume that H-dependent DSS-CP parameters for FCC Ni and H concentration display a similar sigmoidal relation in transition to the saturation condition. For example, the line tension coefficient α_{LE} depends on C_L/C_0 according to

$$\alpha_{LE}(C_L/C_0) = (\alpha_{LE})_{\max} - \frac{(\alpha_{LE})_{\max} - (\alpha_{LE})_{\min}}{1 + \exp\left[-a_{interp}\left(C_L/C_0 - b_{interp}\right)\right]} \tag{17}$$

The assumed interpolative relations between H-affected DSS-CP and C_L/C_0 are plotted in Fig. 3(b)-(d) for α_{LE}, F_0, and s_t^0, respectively. Here, the presence of C_L/C_0 reaching a value of 1 among the elements nearest to the crack tip ensures that the DSS-CP parameters in the vicinity of the notch root are maximally influenced by H, i.e., $\alpha_{LE}(C_L/C_0 = 1) \rightarrow (\alpha_{LE})_{\min}$. However, it's important to note that $C_0 \neq C_{\text{saturation}}$ in our work. In fact, the sigmoidal interpolation described in Eq. (17) doesn't necessitate a particular value of $C_{\text{saturation}}$. We will still encounter $\alpha_{LE}(C_L/C_0 \geq 1) \rightarrow (\alpha_{LE})_{\min}$ when $C_L/C_0 \geq 1$, as seen in Section 5.3 (particularly when employing a higher H-diffusivity). Similarly, for $C_L/C_0 \geq 1$, the values of F_0 is close to $(F_0)_{\max}$ and s_t^0 is close to $(s_t^0)_{\max}$ in the vicinity of the notch root. It is also noted that different interpolation relations can be adopted, e.g., (Xie et al., 2016) suggested a linear relation between H concentration and associated mechanical parameters. We have verified that use of such a linear interpolation will not significantly alter the results ($<\sim$5%) of the crack tip simulations carried out in this work. More physically-based interpolation schemes can explored in future work.

3.4. Two-way coupling algorithm

This section describes the strategy employed to solve the coupled H diffusion and crack tip plasticity problems using ABAQUS. In the nonlinear quasistatic FE solution procedure, a fully implicit backward finite difference algorithm is applied for time integration of the coupled temperature-displacement governing equations (Koric et al., 2009). The solution flowchart of the two-way coupling algorithm is summarized in Fig. 4. For each time step Δt, ABAQUS (Smith, 2009) first provides increments of displacement, Δu, and H concentration field, ΔC_L, serving as initial estimates, and then evolves the fields of stress, strain, and H concentration through the subroutines UMAT and UMATHT, respectively. More specifically, we note that:

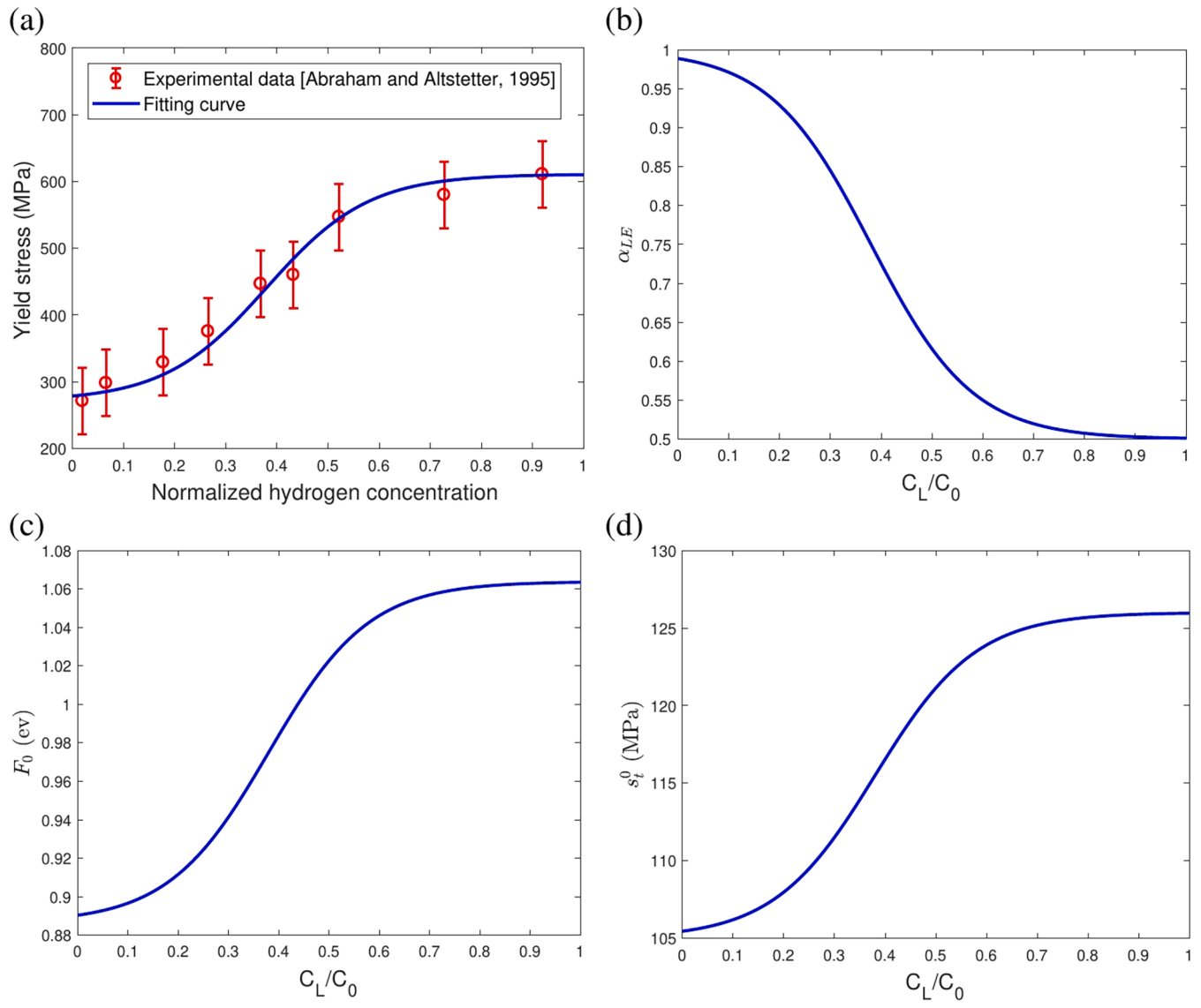

Fig. 3. (a) Experimental yield strength (Abraham and Altstetter, 1995) and its sigmoidal interpolation. Assumed dependence of DSS-CP parameters on the normalized H concentration C_L/C_0 for (b) line tension coefficient, (c) activation energy, and (d) thermal slip resistance. The sigmoidal relations in (b)-(d) are determined by the interpolation in (a).

- In UMAT, DSS-CP parameters are updated based on the updated C_L (i.e., surrogate temperature field), allowing determination of the updated mobile dislocation density $\rho_m^{s\alpha}$ on slip system α and the total dislocation density ρ_{tot} based on Eq. (10).
- UMATHT is then used to solve the fully coupled surrogate temperature-displacement equation. In ABAQUS, UMAT is called before UMATHT, then the updated solution-dependent state variables (STATEV) from UMAT are included with their values passed into UMATHT (Smith, 2009). In our simulation, the mobile dislocation density $\rho_m^{s\alpha}$ is written at each step as a STATEV and passed into UMATHT. Therefore, the trap density N_T (Eq. (10)), the effective H-diffusivity coefficient D_{eff} (Eq. (13)) are updated successively.
- Using URDFIL, we independently calculate the hydrostatic stress gradient $\nabla\sigma_H$, similar to the methodology outlined in (Gobbi et al., 2019). As illustrated in Fig. 4, URDFIL firstly reads the hydrostatic stress data σ_H stored at the end of the last converged time increment, along with the coordinate data of the integration points from the Abaqus output files. The subroutine then computes the spatial stress gradient at the integration points by differentiating the shape functions. This gradient information is subsequently passed to the UMATHT subroutine for use in the next time step (i.e., $t + \Delta t$). This approach assumes that $\nabla\sigma_H$ in the governing equation for transient H diffusion (Eq. (12)) is derived from the last converged time increment. From a numerical perspective, the change in $\nabla\sigma_H$ over each time increment Δt is relatively small, resulting in a negligible effect on solving the deformation gradient and H concentration at each time step. Therefore, this is a typical assumption when solving coupled mechanical and H diffusion problems.

The global Newton-Raphson iteration continues until tolerance is achieved with regard to the residual error criteria for both mechanical and H-diffusion equations, at which point the solution proceeds to the next time step corresponding to $t + \Delta t$. Implementation of Newton's method involves a nonsymmetric Jacobian matrix, as is illustrated in the matrix representation of the coupled equations, i.e.,

$$\begin{bmatrix} K_{uu} & K_{u\theta} \\ K_{\theta u} & K_{\theta\theta} \end{bmatrix} \begin{Bmatrix} \Delta u \\ \Delta\theta \end{Bmatrix} = \begin{Bmatrix} R_u \\ R_\theta \end{Bmatrix} \tag{18}$$

The incremental displacement vector, denoted by Δu, and the equivalent correction to temperature, denoted by $\Delta\theta$ (i.e., ΔC_L in this study), are

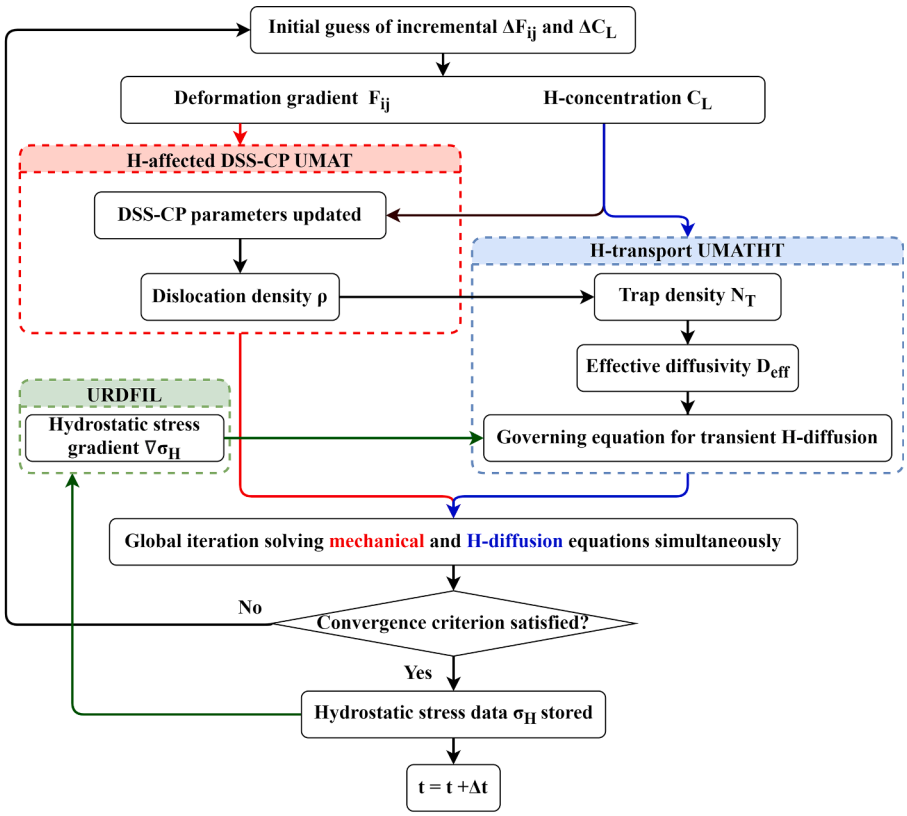

Fig. 4. Flowchart of the two-way incremental coupling algorithm implemented in ABAQUS for each time step, Δt.

calculated alongside submatrices K_{ij} of the fully coupled Jacobian matrix. The mechanical and thermal residual vectors, R_u and R_θ, are then computed, respectively. Solving this system necessitates utilizing an unsymmetric matrix storage and solution scheme, with both mechanical and mass diffusion equations being solved simultaneously. Further details regarding this method are provided elsewhere (Smith, 2009). The "fully coupled thermal-stress analysis" enabling this scheme is available in ABAQUS 6.6 and all later versions.

Note that most studies employing H-transport models (e.g., (Sofronis and McMeeking, 1989) and (Krom et al., 1999)) assume that the mechanical model responses will not be affected by H-effects, i.e., the parameters of mechanical models remain unchanged for various H-concentrations. This means that the parameters of mechanical models remain unchanged for various H-concentrations, resulting in $K_{u\theta}$ always being 0. Enabling the "coupled temp-displacement" in ABAQUS (i.e., allowing non-zero $K_{u\theta}$) will not affect the computational time in such cases. In contrast, the present two-way coupled modeling framework accounts for the direct dependence of the DSS-CP parameters on H-concentration; these parameters (e.g., α_{LE}) are updated with ΔC_L for each incremental time step Δt. This leads to $K_{u\theta} = \partial F_u\left(F_0(\theta), s_t^0(\theta), \alpha_{LE}(\theta)\right)/\partial\theta \neq 0$, which influences the computational time. Therefore, in the ABAQUS global iteration, it is necessary to allow $K_{u\theta}$ to be non-zero for faster numerical convergence.

4. Results

4.1. Crack tip distribution of H concentration and DSS-CP parameters

In this section we analyze the results from the two-way coupling algorithm including: (i) field distribution and evolution of the H lattice concentration, C_L, (ii) distribution and evolution of DSS-CP parameters that are affected by C_L/C_0, and (iii) distribution of the H trap concentration C_T. Fig. 5(a) shows the normalized distribution of C_L/C_0 at loading times of $t = 10$ s and 51 s, corresponding to applied stress intensity factors of $K_I = 1.96$ MPa$\sqrt{\text{m}}$ and 10 MPa$\sqrt{\text{m}}$, respectively. It is seen that H initially accumulates near the crack tip and subsequently diffuses to enhance coverage of the crack tip region with time. Fig. 5(b) shows the evolution of line tension coefficient α_{LE} at loading times of $t =$ 10 s and 51 s. The field of α_{LE} follows that of crack tip H, with a low value of 0.5 at the notch root and a far field value of 1.0 corresponding to the absence of H. The other H-affected DSS-CP parameters, including the thermal resistance s_t^0 and activation energy F_0, evolve similarly with change of local H lattice concentration, C_L.

Fig. 6 illustrates the distribution of normalized H trap concentration (C_T/C_0) at a loading time of $t = 51$ s upon reaching an applied stress intensity factor of $K_I = 10$ MPa$\sqrt{\text{m}}$. The highest C_T/C_0 values are observed in the elements near the notch root, reaching $\sim 10^{-2}$, and exhibit a rapid decrease with the increasing distance from the crack tip. We have chosen a smaller maximum value of C_T/C_0 (i.e., 10^{-3}), such that the gray area near the crack tip indicates that C_T/C_0 exceeds 10^{-3}. This adjustment ensures a clearer representation of the size of the region with higher C_T/C_0 values near the crack tip. Additionally, it enables a comparison of contour sizes with those of C_L/C_0, as illustrated in Figs. 5 and 6.

Near the crack tip, the sum of dislocation densities $\rho_{tot} = \eta_m \sum \rho_m^{s\alpha}$ reads $\sim 10^{15}$ m^{-2}. Based on Eq. (10), the corresponding peak values of trap density N_T near the crack tip are $\sim 10^{24}$ m^{-3}. This N_T value for FCC Ni is comparable to that of previous studies (Sofronis and McMeeking, 1989) in which BCC iron exhibited N_T values of $\sim 10^{22}$ m^{-3} under 20 % effective plastic deformation. However, owing to the lower trap binding energy W_B of 10 kJ/mol in Eq. (6) for FCC in comparison to BCC crystals (50 kJ/mol), combined with the shorter time for H ingress (i.e., 51 s), C_T/C_0 values are lower in this work for FCC than the literature values for BCC crystals. Additionally, the C_T/C_0 profile shares similarities with the pattern of $\sum \rho_m^{s\alpha}$. The lower stress intensity factor used in our study compared to the literature value ($K_I = 100$ MPa$\sqrt{\text{m}}$ in (Sofronis and

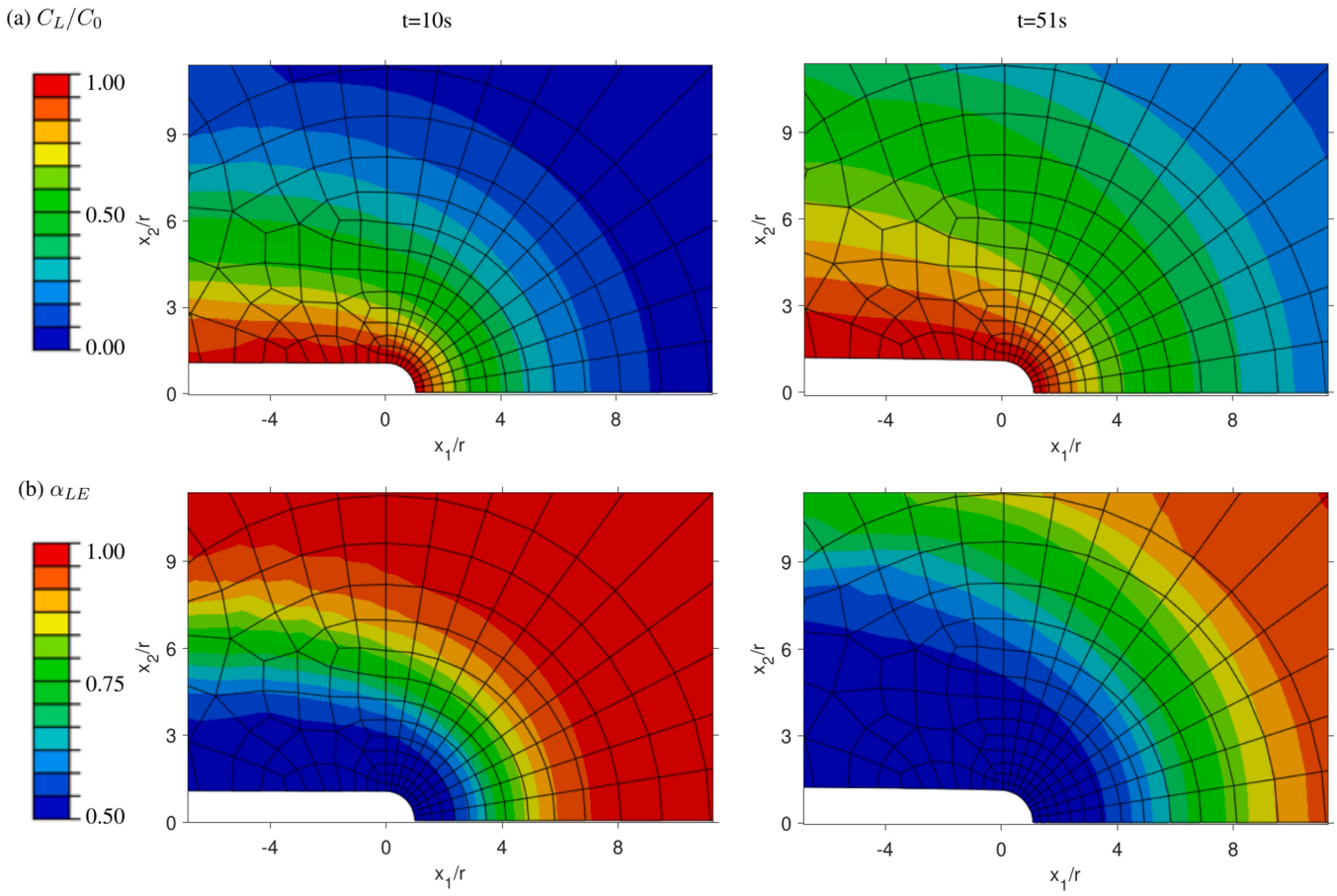

Fig. 5. Contours of (a) normalized H lattice concentration C_L/C_0 and (b) line tension coefficient α_{LE} at $t = 10$ s (left column) and 51 s (right column), near the notch root. The far-field monotonic loading is applied throughout this work, with $K_I = 10\,\mathrm{MPa}\sqrt{\mathrm{m}}$, applied over a total rise time of 51 s. The local value of α_{LE} at each integration point is updated based on the local value of C_L. The notch radius is denoted by r.

McMeeking, 1989)) leads to a smaller area of $\sum \rho_m^{s\alpha}$ and C_T/C_0. As a result, the C_T/C_0 values for FCC crystals in this work near the crack tip are significantly reduced compared to the literature for BCC crystals.

The effective diffusion constant D_{eff} in Eq. (13) just at the notch root can be expressed as follows, where C_L near the crack tip is approximately equal to C_0: $D_{eff} \approx D/[1 + C_T/C_0(1 - \theta_T)]$. The peak value of $C_T/C_L \approx C_T/C_0$ is $\sim 10^{-2}$, and θ_T near the crack tip is also $\sim 10^{-2}$. Therefore, changes in crack tip dislocation density $\sum \rho_m^{s\alpha}$ only result in a minimal ($\sim$1%) variation in D_{eff} near the notch root. In the far field, D_{eff} is closely aligned with the H-diffusivity (D) as $C_T \to 0$.

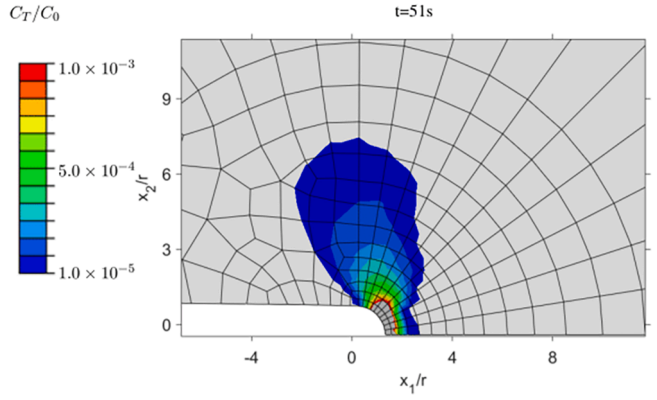

Fig. 6. Contours of normalized H trap concentration C_T/C_0 at $t = 51$ s. The gray regions near the crack tip indicate C_T/C_0 values greater than 10^{-3}, whereas the gray regions distant from the crack tip represent C_T nearly equal to 0.

4.2. Influence of H on plastic strain distribution near the crack tip

The distribution of effective plastic strain $\varepsilon_p^{eff} = \sqrt{2/3\left(\varepsilon_{ij}^p \varepsilon_{ij}^p\right)}$, as well as that of the plastic shear strain γ^α on individual slip systems, are computed in the vicinity of crack tip. The asymptotic analysis of the stress and deformation fields at the tip of a stationary crack is performed in FCC single crystals subjected to Mode I loading under plane strain conditions in (Patil et al., 2008b; Rice, 1987). In these previous studies, the behavior of ductile single crystals was modeled as rigid-ideal plastic, and slip line field solutions were sought within a small-strain framework. For the FCC single crystal, the plane of the crack is taken to coincide with the (010) plane, and the crack front was chosen to lie along $[\bar{1}01]$ direction (the same as used in the present work). Three combinations of slip systems, i.e., conjugate pair $(1\bar{1}1)[110]$ & $(1\bar{1}1)[011]$, $(\bar{1}11)[101]$ & $(11\bar{1})[101]$, and $(111)[1\bar{1}0]$ & $(111)[01\bar{1}]$, are considered here, resulting in plane strain deformation, while other slip systems remain inactive.

Fig. 7(a) shows contours of ε_p^{eff} at $t = 51$ s (i.e., peak loading condition of $K_I = 10$ MPa$\sqrt{\mathrm{m}}$) using the DSS-CP model without H-effects. Fig. 7(b)-(d) show the plastic shear field γ^α of the active slip systems without H, pertaining to the conjugate slip system pairs $(1\bar{1}1)[110]$ & $(1\bar{1}1)[011]$, $(\bar{1}11)[101]$ & $(11\bar{1})[101]$ and $(111)[1\bar{1}0]$ & $(111)[01\bar{1}]$ for (b), (c) and (d), respectively. In Fig. 7(b)-(d), R_i ($i = 1,2,3$) represents the radial distance along the slip line direction, while r denotes the notch radius. R_1, R_2, and R_3 are associated with the aforementioned three pairs

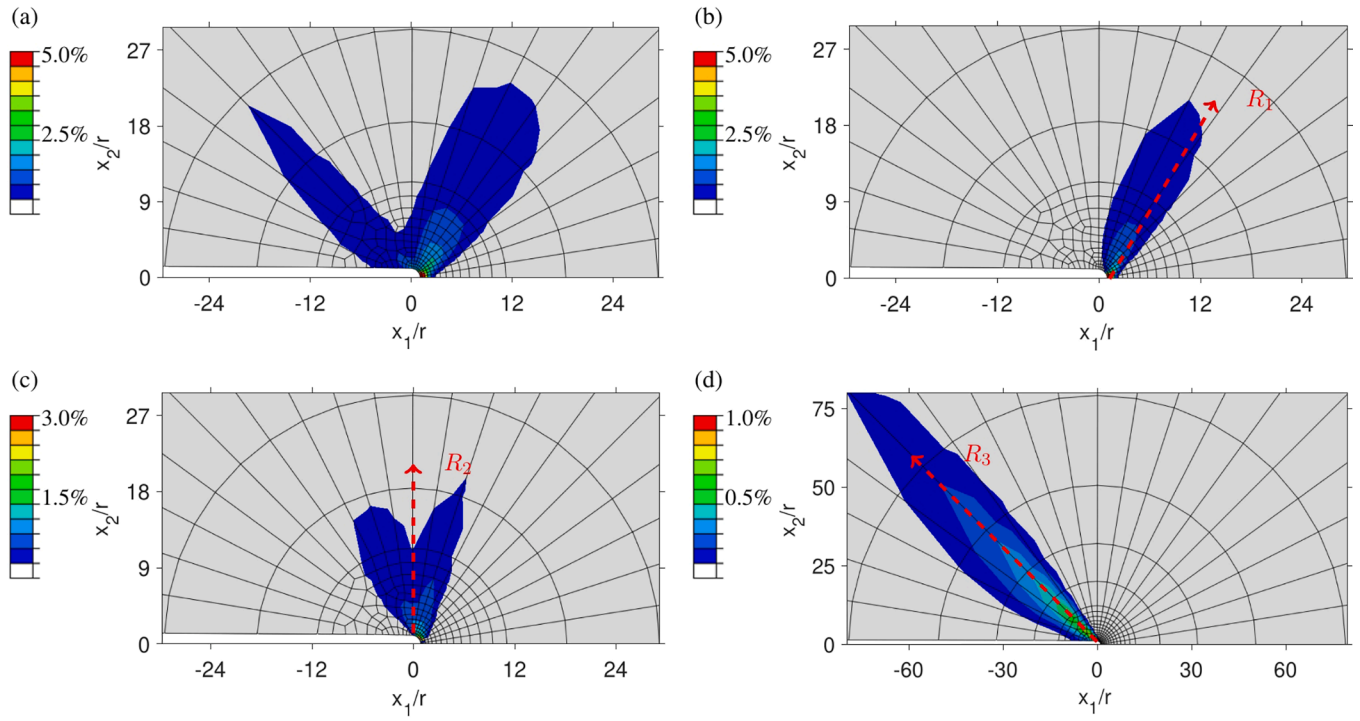

Fig. 7. (a) Contour of effective plastic strain ε_p^{eff} simulated using the DSS-CP model without H-effect; (b)-(d) Contour of plastic shear strain γ^{α} in the active slip system without H-effect. (b), (c) and (d) respectively pertain to the conjugate pair of slip systems $(1\bar{1}1)[110]$ & $(1\bar{1}1)[011]$, $(\bar{1}11)[101]$ & $(11\bar{1})[101]$ and $(111)[1\bar{1}0]$ & $(111)[01\bar{1}]$. In (b)-(d), R_i (i.e., R_1, R_2, and R_3 corresponding to the aforementioned three pairs of conjugate slip systems) and r denote the radial distance along the slip line direction and notch radius, respectively.

of conjugate slip systems. These three slip line traces are inclined at 54.7°, 90.0°, and 125.3°, respectively, with respect to the positive x_1 axis as indicated in Fig. 7 (b)-(d). Note also that the contours of effective plastic strain and plastic shear strain are not entirely commensurate with the literature (e.g., (Patil et al., 2008b)). This might be associated with different applied loading rates and CP constitutive laws used, as the more recent DSS-CP model developed by (Castelluccio and McDowell, 2017) was essential to providing more physically-based description of work hardening, including cyclic loading effects.

Fig. 8(a) shows the effective plastic strain ε_p^{eff} versus the normalized distance along the crack extension direction, x_1/r, where r denotes the notch radius. Fig. 8(b)-(d) presents γ^{α} on the active slip system versus the normalized distance, R_i/r, where R_i denotes the radial distance from the crack tip. The red dashed arrows plotted in Fig. 8(b)-(d) indicate the angle along with the radial distance R_i ($i = 1,2,3$) measured in Fig. 7(b)-(d), for the conjugate pair of slip systems $(1\bar{1}1)[110]$ & $(1\bar{1}1)[011]$, $(\bar{1}11)[101]$ & $(11\bar{1})[101]$ and $(111)[1\bar{1}0]$ & $(111)[01\bar{1}]$, respectively. The results with and without H are compared in Fig. 8.

It is found that H enhances the maximum effective plastic strain ε_p^{eff} by about 40% compared to the baseline case without H in the vicinity of the crack tip and increases the gradient of plastic strain near the crack tip. Furthermore, Fig. 8(a) shows that the size of crack tip plastic zone does not increase markedly in the presence of H. The rapid decrease in strain with increasing distance from the crack tip indicate that H mainly enhances the localization of the plastic deformation ahead of the crack tip in an FCC single crystal. In Fig. 8(b), the peak plastic shear γ^{α} is observed at levels of $\sim$ 0.11 with H versus $\sim$ 0.08 without H. Peak γ^{α} values on the other active slip systems in Fig. 8(c) and 8(d) display a similar trend, i.e., an enhancement of the near crack tip slip system shear is observed. In summary, we observe an enhancement of near crack tip plasticity (both the effective plastic strain ε_p^{eff} and the plastic shear strain γ^{α}) in the presence of H, which is consistent with experimental data reported for Ni single crystals with and without H (Sun et al., 1995). Additionally, experiments demonstrate that the plastic zone size does not significantly extend under the influence of H, consistent with our predictions. Refer to Appendix A for the available experimental data supporting the trend of our predictions.

4.3. H effect on crack tip opening displacement (CTOD)

Crack tip opening displacement (CTOD) is defined as the separation between opposing faces of a crack tip at the 90° intercept position. Experiments by (Sun et al., 1995) have indicated that the presence of H significantly increases the CTOD for Ni single crystals. The augmentation of CTOD is widely attributed to the enhanced near crack tip plasticity (i.e., HELP mechanism) and the increased crack growth rate in the presence of H. In this study, the influence of H on CTOD, δ_t. using the two-way coupled DSS-CP and H-transport models is summarized in Table 1. The δ_t values are 11.0 μm and 12.0 μm at $t = 51$ s without/with H effects, respectively, i.e., CTOD increases by $\sim$ 8.2% with H effect. Furthermore, the normalized δ_t/r is calculated, where $r = 5$ μm represents the notch radius. The respective values of normalized δ_t/r are 2.2 and 2.4 without/with H. Therefore, the simulations in this work capture the trend of experimental observations of increased CTOD with introduction of H.

Experimental data (see Appendix A) reveal that the presence of H has an insignificant effect on CTOD enhancement under low loading magnitudes, i.e., $K_I \leq 10$ MPa$\sqrt{m}$. In contrast, for larger loading magnitudes, such as $K_I = 30$ MPa$\sqrt{m}$, significant disparities in CTOD are observed, with readings of 4 μm and 30 μm without/with H, respectively. Hence, our predictions are consistent with experiments with relatively small load amplitude ($K_I \leq 10$ MPa$\sqrt{m}$). We do not pursue the higher load levels in this work owing to the larger scale plasticity and need to incorporate a crack growth methodology to do so.

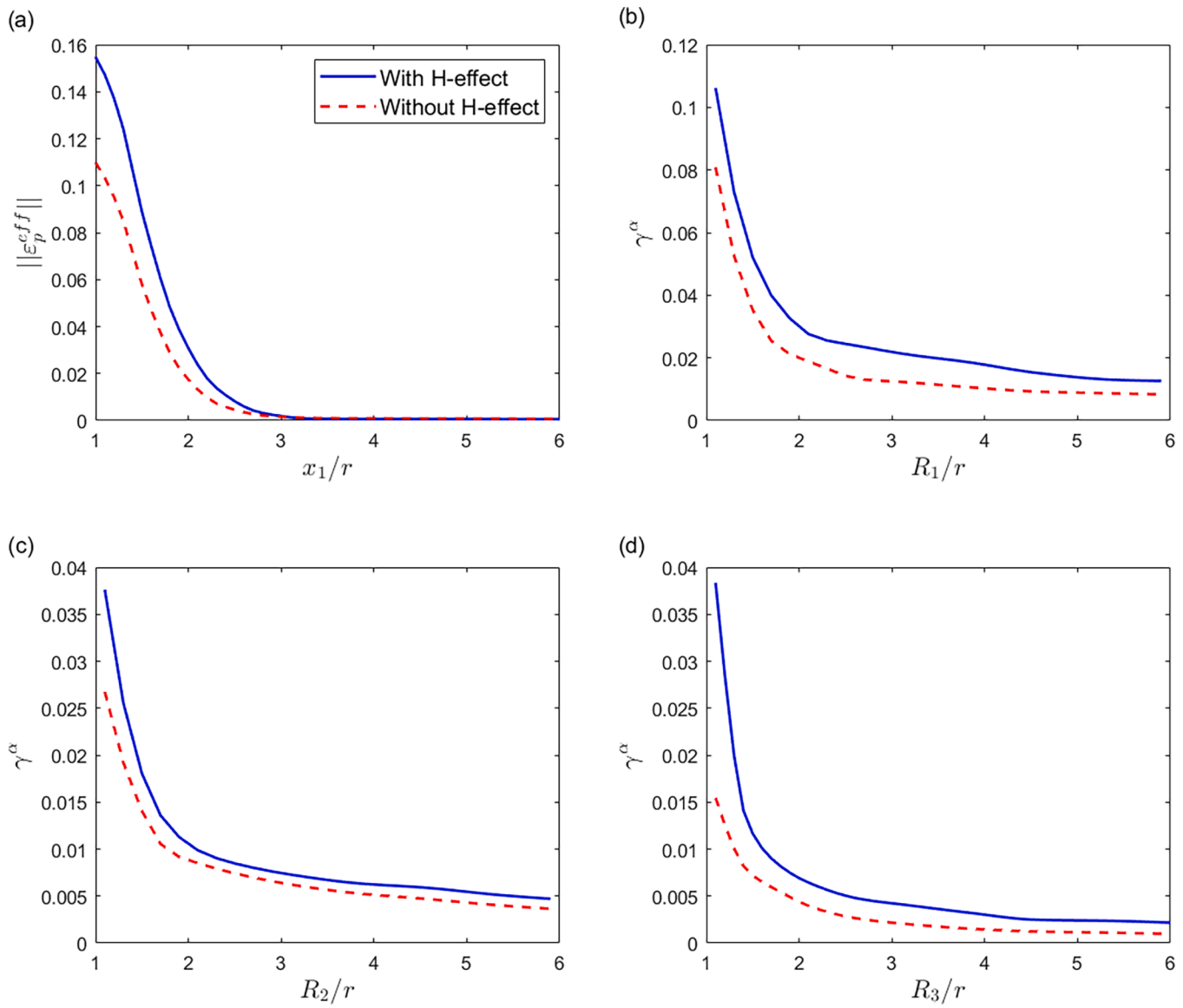

Fig. 8. Enhancement of crack tip plasticity with H-effects. (a) Effective plastic strain as a function of the normalized radial distance x_1/r in advance of the crack. (b)-(d) Plastic shear strain γ^α as a function of the normalized radial distance along the slip line direction (indicated by the dashed red arrow in Fig. 7). (b), (c) and (d) pertain to the conjugate pair of slip systems $(1\bar{1}1)[110]$ & $(1\bar{1}1)[011]$, $(\bar{1}11)[101]$ & $(11\bar{1})[101]$, and $(111)[1\bar{1}0]$ & $(111)[01\bar{1}]$, respectively.

5. Discussion and sensitivity studies

Our results discussed in the last section demonstrate the feasibility of applying the H-coupled DSS-CP model to capture relevant observed trends regarding enhanced crack tip plasticity in the presence of H. These trends are consistent with experimental observations, e.g., (Hatano et al., 2014; Sun et al., 1995), demonstrating H-enhanced plastic flow localization at the mesoscale in the presence of H. It is noted that enhancement of crack tip plasticity with H in these simulations has the effect of enhancing individual slip system shears, as would be expected based on the DSS-CP parameter dependencies for each slip system. However, the levels of intensification of the slip system plastic shearing near the crack tip in these examples are not as high as might be expected based on experimental results (e.g., (Hatano et al., 2014; Robertson et al., 2015)). We note that the simulations with H reported in this work pertain to specific assumed initial and boundary conditions; high H levels are obtained only near the crack tip, as shown in Fig. 5(a); with longer rise times or cyclic loading over a number of cycles, H would continue to diffuse to build up higher levels of C_L further from the crack tip. With this as a caveat, one might reasonably conclude that consideration of effects of H only through direct dependence of crystal plasticity model parameters as undertaken here is unlikely to produce the degree of crack tip strain localization that is observed experimentally. To reinforce this conclusion, we next pursue sensitivity studies of the dependence of these model parameters on H to assess whether it is possible to fully capture H-induced strain localization with such a framework, absent additional physics.

Sensitivity studies of enhanced crack tip plasticity (or "crack tip plastic strain localization/intensification") with regard to H-sensitive model parameters are conducted to explore the degree to which effects

Table 1
Crack Tip Opening Displacement (CTOD) and normalized CTOD values under H-free and H-affected conditions, predicted by the two-way coupled DSS-CP and H-transport models at a loading time of 51 s.

	CTOD δ_t (μm)	Normalized CTOD δ_t/r
Without H-effect	11.015	2.203
With H-effect	11.960	2.392

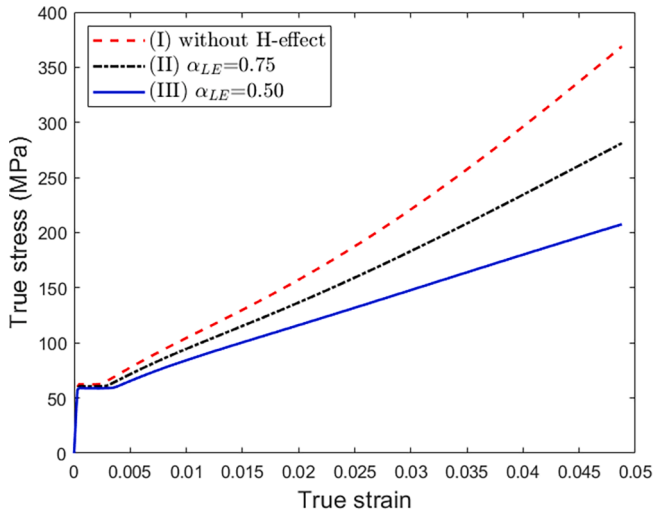

Fig. 9. True tensile stress–strain curves for several values of the line tension coefficient α_{LE}, leading to reduction of the post-yield strain hardening rate with H.

of H can be addressed with the present model. H-affected reduction of the rate of strain hardening rate and H-enhanced yield strength will be analyzed in Section 5.1 and Section 5.2, respectively. Section 5.3 explores the effect of H-diffusivity on H-enhanced crack tip plasticity, making use of the two-way coupling algorithm for DSS-CP and H-diffusion models. Finally, in Section 5.4, the differences in model responses between the two-way coupling algorithm and the assumption of homogeneous H distribution assumption (i.e., assuming homogeneous H distribution throughout simulation) will be discussed.

5.1. Parameter sensitivity: H effects on reduced rate of strain hardening

Reducing α_{LE} leads to a decrease of the rate of strain hardening. In this section, we hold F_0 and s_t^0 fixed. Fig. 9 shows the DSS-CP model responses for Ni single crystals loaded uniaxially along [1 0 0] with several values of α_{LE}, resulting in different strain hardening rates: (I) $\alpha_{LE} = 1.0$, corresponding to the case without H, (II) $\alpha_{LE} = 0.75$, and (III) $\alpha_{LE} = 0.5$. Cases (II) and (III) represent true tensile stress–strain curves influenced by H at an exceptionally high and uniform H concentration (i.e., $C_L/C_0 = 1$), consistent with the local H concentration near the notch root in the two-way coupled simulation.

Fig. 10 illustrates the evolution of α_{LE} at loading times of (a) of $t = 10$ s corresponding to applied $K_I = 1.96$ MPa$\sqrt{\text{m}}$ and (b) $t = 51$ s with $K_I = 10$ MPa$\sqrt{\text{m}}$. Case (I) corresponds to α_{LE} remaining constant at 1.0, representing the scenario without H. $(\alpha_{LE})_{\min}$ in Eq. (17), which corresponds to extremely high H concentration at the crack tip, is selected for case (II) with a value of 0.75 and for case (III) 0.5. The continuous variation of α_{LE} is associated with the evolving levels C_L/C_0, as H progressively diffuses into the interior of the Ni single crystal during the loading process. This diffusion phenomenon results in an elevated C_L/C_0 near the crack tip, as shown in Fig. 5(a). Therefore, in case (II) and case (III), α_{LE} values near the crack tip decrease progressively. Here, we choose the conjugate pair of slip systems $(\bar{1}11)[101]$ & $(11\bar{1})[101]$ as an example to illustrate the temporal behavior of α_{LE}, by plotting α_{LE} as a function of the normalized radial distance along the slip line direction R_2/r. We have verified that the variations of α_{LE} in the x_1 direction and the R_1 and R_3 directions display a similar pattern.

Fig. 11(a) plots the effective plastic strain with respect to the normalized radial distance ahead of the crack front for the two-way coupled problem, for Case (I) $\alpha_{LE} = 1.0$ (baseline without H), Case (II) $(\alpha_{LE})_{\min} = 0.75$ near the notch root, and Case (III) $(\alpha_{LE})_{\min} = 0.5$. The maximum effective plastic strain levels are ~ 11 %, ~14% and ~ 17% ahead of the notch root, respectively, for Cases (I), (II), and (III). Fig. 11 (b) illustrates the plastic shear strain γ^{α} pertain to the conjugate pair of slip system $(\bar{1}11)[101]$ & $(11\bar{1})[101]$ as a function of its normalized radial distance along the slip line direction R_2/r. Similar to the case of effective plastic strain, when the minimum values of α_{LE} decrease, the enhancement of the maximum γ^{α} is observed. Additionally, we have verified that the other conjugate pairs of slip systems exhibit a similar trend. Clearly, reduction of the strain hardening rate achieved via reduction of the line tension coefficient α_{LE} with H is most effective in promoting crack tip strain localization. Therefore, we conclude that based on a parametric study over a range of H-influence of parameters of the DSS-CP, the reduced rate of strain hardening is dominant in enhancing localized crack tip plasticity.

5.2. Parameter sensitivity: H-enhanced yield strength

In contrast to the influence of H on α_{LE} in decreasing the strain hardening rate, H-induced increase of yield strength is achieved by increasing F_0 and s_t^0 in the present model. Fig. 12(a) considers several combinations of F_0 and s_t^0 values in the DSS-CP model, without changing the line tension coefficient α_{LE}. This leads to different H-enhanced yield

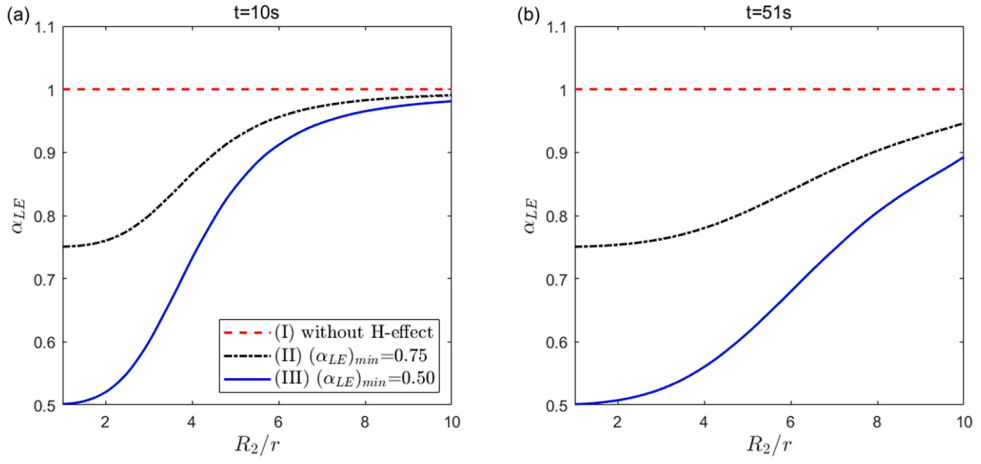

Fig. 10. Evolution of the line tension coefficient α_{LE} as a function of the normalized radial distance along the slip line direction R_2/r: (a) at $t = 10$ s; (b) at $t = 51$ s for the cases (I) without H effect, i.e., $\alpha_{LE} = 1.0$ throughout the simulation, (II) $(\alpha_{LE})_{\min} = 0.75$, and (III) $(\alpha_{LE})_{\min} = 0.50$ at the notch root. Here, R_2 is an example which pertains to the conjugate pair of slip systems $(\bar{1}11)[101]$ & $(11\bar{1})[101]$; Profile of $(\alpha_{LE})_{\min}$ along R_1/r and R_3/r display a similar trend. The α_{LE} is updated based on the C_L distribution.

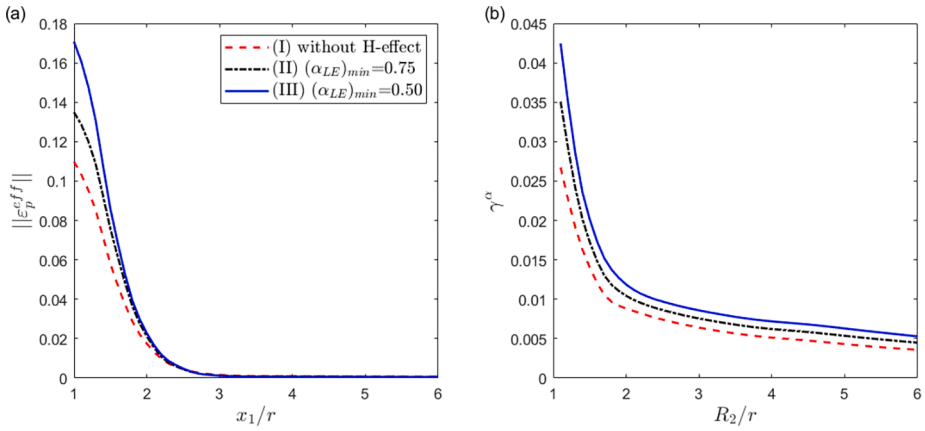

Fig. 11. (a) Effective plastic strain as a function of the normalized distance ahead of the crack front for different cases of α_{LE} profiles, i.e., (I) without H-effect, (II) $(\alpha_{LE})_{\min} = 0.75$ and (III) $(\alpha_{LE})_{\min} = 0.50$; (b) Plastic shear strain γ^{α} pertain to the conjugate pair of slip system $(\bar{1}11)[101]$ & $(11\bar{1})[101]$ as a function of its normalized radial distance along the slip line direction R_2/r. A greater degree of reduction of the strain hardening rate with H leads to more significant enhancement of crack tip plasticity. The initial boundary value has been outlined in Section 4 with $t = 51$ s rise time to a peak loading condition of $K_I = 10\,\text{MPa}\sqrt{\text{m}}$ which are applied to all the other simulations throughout the work.

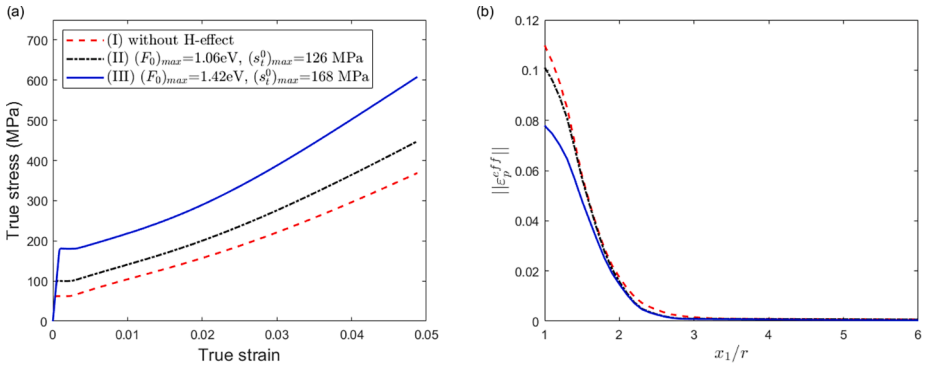

Fig. 12. (a) True tensile stress–strain curves with different activation energy and thermal slip resistance, leading to various H-enhanced yield strength. These curves are obtained using the DSS-CP model for Ni single crystals, loaded in uniaxial tension along the [100] direction. Cases (II) and (III) correspond to the H-affected stress–strain curves with extremely high uniform H concentration (i.e., $C_L/C_0 = 1$ throughout the field). (b) Effective plastic strain as a function of the normalized radial distance along the crack direction for the two-way coupled problem.

strength levels, σ_Y, in true tensile stress–strain response for Ni single crystals, loaded along the [100] direction with high uniform H concentration (i.e., $C_L/C_0 = 1$) throughout the field. In reality, such high concentrations of H would only occur very near the crack tip). Several cases are considered as follows: (I) $F_0 = 0.89$ eV, $s_t^0 = 105$ MPa, leading to $\sigma_Y \sim 50$ MPa, corresponding to the case without H effect; (II) $F_0 = 1.06$ eV, $s_t^0 = 126$ MPa (F_0 and s_t^0 increased by 20%), leading to $\sigma_Y \sim 100$ MPa; (III) $F_0 = 1.42$ eV, $s_t^0 = 168$ MPa (F_0 and s_t^0 increased by 60%), leading to $\sigma_Y \sim 200$ MPa. The parameter combination (II) is adopted since experiments indicate that the yield strength should be approximately doubled to achieve the strongest effect at high H concentration (Abraham and Altstetter, 1995; Xie et al., 2016). To further investigate the role of yield strength in enhancement of crack tip plasticity, combination (III) is also considered. It is worth noting that in combinations (II) and (III), strain hardening rates are also enhanced slightly due to the higher values of F_0.

In our crack tip simulation employing the two-way coupling algorithm, the distributions of F_0 and s_t^0 resemble that observed in Fig. 10 for α_{LE}. Specifically, the alterations in DSS-CP parameters are prominent only near the notch root; in regions distant from the crack tip, the DSS-CP parameters remain unaffected. Fig. 12(b) plots the model responses of effective plastic strain versus the normalized radial distance ahead of the crack front. The peak effective plastic strain levels are ~ 11%, ~10% and ~ 8% ahead of the notch root, respectively, for the parameter combinations (I), (II) and (III). A similar trend is seen for γ^{α}, i.e., enlarged F_0 and s_t^0 leads to increase of σ_Y and results in reduced magnitude of crack tip slip system shears γ^{α}. Therefore, one can conclude that accounting only for H-induced increase of yield strength cannot properly explain crack tip strain intensification/localization phenomena, even though the increase of yield strength is fully expected from a physical perspective owing to the influence of H, and it is experimentally observed (Xie et al., 2016). This clearly demonstrates the importance of a reduced rate of strain hardening after initial yielding to describe H-enhanced crack tip plasticity, as discussed in Section 5.1.

5.3. Parameter sensitivity: H-Diffusivity

In crack tip simulations in this work, the H-affected DSS-CP model is two-way coupled with the H-transport model, accounting for (i) effects of mechanical deformation on H transport and (ii) effects of H on mechanical deformation. Previous H-diffusion models (e.g., (Sofronis and McMeeking, 1989)) have systemically considered effects of the mechanical deformation near the crack tip on the H-concentration. In this section, we will explore the effects of H-distribution on the crack tip plasticity. As discussed in Section 4.1, the changes in $\sum \rho_m^{s\alpha}$ near the crack tip result in only ~ 1% variation in H distribution. Furthermore, the impact of $\nabla\sigma_H$ on H distribution is also limited to ~ 3% (see Appendix D). Thus, the alterations in $\sum \rho_m^{s\alpha}$ and $\nabla\sigma_H$ within this study exhibit relatively minor effects on H distribution. In order to significantly alter the distribution of H concentration near the crack tip and

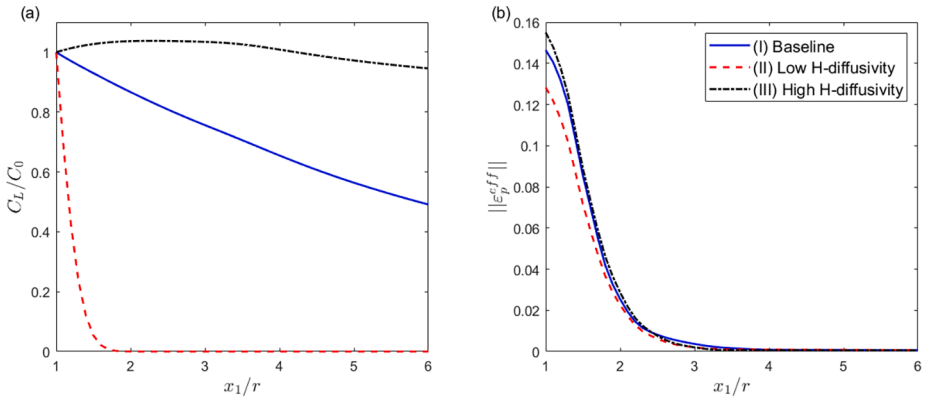

Fig. 13. (a) Normalized H-concentration as a function of the normalized distance ahead of the crack front with various H-diffusivity D assigned. For the two-way coupled problem, the same initial boundary value has been used in Section 4 with $t = 51$ s rise time to a peak loading condition of $K_I = 10\,\mathrm{MPa}\sqrt{\mathrm{m}}$. (b) Effective plastic strain as a function of the normalized distance ahead of the crack front. Higher H-diffusivity leads to more significant enhancement of the near crack tip plasticity.

also gain a comprehensive understanding of the influence of H-diffusivity D on the distribution of plastic strain fields, we employ three distinct H-diffusivity scenarios as follows: (I) baseline $D = 5 \times 10^{-13}\,\mathrm{m}^2/\mathrm{s}$; (II) low H-diffusivity $D = 2 \times 10^{-16}\,\mathrm{m}^2/\mathrm{s}$ for the FCC SS forged Nitronic 40 used in (Dadfarnia et al., 2015); (III) high H-diffusivity $D = 1.27 \times 10^{-8}\,\mathrm{m}^2/\mathrm{s}$ for the BCC iron used in (Sofronis and McMeeking, 1989). The H-diffusivity adopted in Case (I) is used to produce the simulation results in Section 4.1. Fig. 13(a) shows H-diffusion model responses with various values of H-diffusivity assigned, resulting in different sizes of H-affected crack tip zones at $t = 51$ s.

Fig. 13(b) plots the effective plastic strain versus the normalized radial distance ahead of the crack tip. The peak effective plastic strain levels are ~ 15%, ~ 13%, and ~ 16% ahead of the notch root, respectively, for Cases (I), (II), and (III). Thus, we effectively demonstrate numerical implementation of the two-way coupling algorithm in FEM, evident through the observed influence of H-distribution on mechanical model responses. Moreover, from a physical standpoint, higher H-diffusivity corresponds to more pronounced H effects in the model, leading to a more substantial enhancement of near crack tip plasticity. However, we note that the maximum effect of enhancement evident from Fig. 13(b) is not substantial compared to experimental observations of H diffusion effects on crack tip strain localization (e.g., (Hatano et al., 2014; Robertson et al., 2015; Wang et al., 2017)). This points to limitations of a constitutive crystal plasticity framework that considers only the effects of H through values of certain physically-based model parameters.

It should also be noted that the finding regarding the general importance of the two-way coupling algorithm has relevance to other systems as well, which can be studied in future work. For example, cyclic loading over a number of cycles (or a longer rise time subjected) will allow H to diffuse a longer time near the notch root, leading to an enlarged H-effected zone and likely a stronger HE phenomena, compared to the monotonic loading condition studied in this work. Similarly, elevated temperature and deformation-induced mobile dislocation network will also promote higher H mobility (Dadfarnia et al., 2015).

Severe deformation near the crack tip can lead to localized strain-induced martensitic transformation from the FCC structure. Martensite exhibits a much higher H-diffusivity compared to FCC (e.g., $2.4 \times 10^{-13}\,\mathrm{m}^2/\mathrm{s}$ and $5.5 \times 10^{-15}\,\mathrm{m}^2/\mathrm{s}$ at 353 K for prestrained 304 Stainless Steel (SS) and solution-treated 304 SS, respectively) (Murakami et al., 2008). An additional experiment by (Saintier et al., 2011) demonstrated that 304 SS exhibits higher H solubility and H diffusivity in deformed regions, which was attributed to cyclic plastic activity at the crack tip. It is also observed that the crack growth rate with H-charging for 304 SS is on the order of three times faster than that of 316L SS which does not undergo substantial martensitic transformation (Murakami et al., 2008). The two-way coupling algorithm enables the simulation of such mechanisms, i.e., the expansion of the H-affected zone resulting in stronger enhanced crack tip plasticity, along with a corresponding accelerated

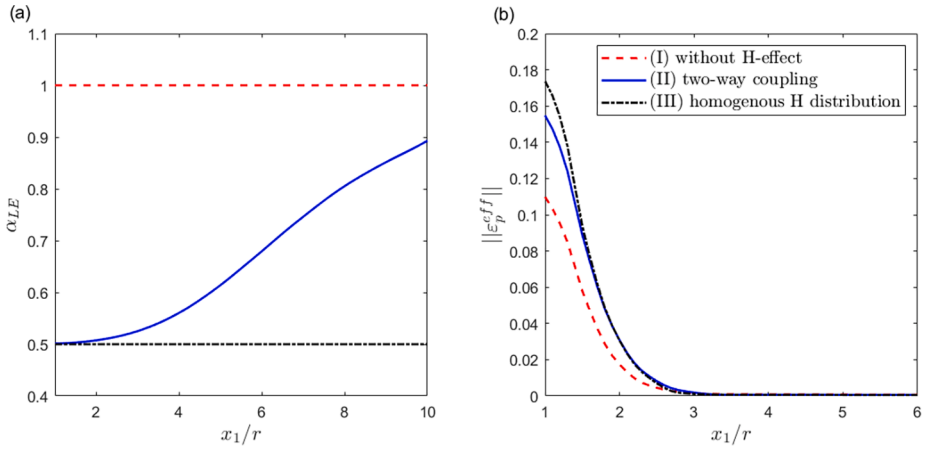

Fig. 14. (a) Line tension coefficient α_{LE} as a function of x_1/r at $t = 51$ s for the three cases: (I) without H-effect, i.e., α_{LE} remains constant at 1.0; (II) two-way coupling algorithm, i.e., α_{LE} updated based on the evolution of C_L; (III) homogenous H-distribution assumption resulting in a constant α_{LE} of 0.5 throughout simulation. (b) Model responses of the effective plastic strain in terms of x_1/r for these three cases.

development of dislocation substructure. In other words, our simulation shows that increased H-diffusivity enhances the HELP mechanism, which might ultimately contribution to the accelerated fatigue crack growth rate (Neeraj et al., 2012; Robertson et al., 2015). Therefore, our work offers a possible numerical strategy to explore the effect of martensitic phase transformation on H-effect for SS 304, if this is to be included. To our knowledge, there are no previously published modeling frameworks that enable the investigation of the impact of H-diffusivity on the mechanical behavior at the crack tip. Recall that previous theoretical/computational studies, e.g., (Krom et al., 1999; Kumar and Mahajan, 2020) have focused on the role of enhanced crack tip plasticity in promoting the generation of H traps (e.g., dislocations cores), leading to a higher H-concentration.

5.4. *Effect of the two-way coupling algorithm compared to homogeneous H distribution*

In this study, we introduced a novel two-way coupling approach between the recently developed DSS-CP model and H-transport model, enabling the simultaneous computation of mechanical and H diffusion equations at each time increment. On the other hand, many existing mechanical models addressing H effects assume a homogenous and constant H distribution within the specimen, discussing its impact on the mechanical behavior (e.g., (Castelluccio et al., 2018; Yuan et al., 2020)), referred to as the "homogeneous H distribution" case. In this section, we will investigate how mechanical responses differ between the two-way coupling algorithm and the homogeneous H distribution. Fig. 14(a) shows the α_{LE} distribution at $t = 51$ s for three cases: (I) without H effect, (II) employing the two-way coupling algorithm, and (III) assuming a homogeneous H distribution. In case (III), the entire mesh assumes a uniform and saturated H concentration ($C_L/C_0 = 1.0$), leading to a constant α_{LE} distribution of 0.5 throughout the simulation. Conversely, in case (I), without H effect, α_{LE} remains uniform at 1.0. In case (II), the non-uniform distribution of α_{LE} near the crack tip results from variations in C_L/C_0. The dashed lines in Fig. 14(a) outline the α_{LE} distribution along the crack tip extension direction (x_1/r) at 51 s, similar to Fig. 10(b), illustrating the α_{LE} distribution along R_2/r. The contour of F_0 and s_t^0 in the (II) two-way coupling display a similar evolution compared to those of α_{LE} and are not plotted here for the sake of simplicity.

As depicted in Fig. 14(b), case (III) leads to a more pronounced enhancement of crack tip plasticity, with a peak value of $\sim$ 17%. The responses of equivalent plastic deformation for cases (I) and (II) are consistent with Fig. 8(a), corresponding to $\sim$ 11% and $\sim$ 15%, respectively. A similar trend is observed in the plastic shear strain γ^{α} on active slip systems, where the peak value of γ^{α} in (III) surpasses that in (II). This observation highlights the distinct model responses between the (II) two-way coupling algorithm and the (III) homogeneous H-distribution. As the crack opens, the (II) two-way coupling progressively modifies the H affected DSS-CP model parameters, while (III) assumes model parameter remain unchanged, which leads to more pronounced localization of the plastic strain. Therefore, the development of (II) the two-way coupling algorithm potentially contributes to in-depth analysis of the bidirectional coupling between H distribution and the H-affected mechanical field.

6. Conclusions

This work focuses on two-way coupling DSS-CP and H transport near an initially blunted crack tip in a single crystal level for FCC metals. Effects of H are considered on (i) enhanced yield strength owing to H effects in coupling with higher activation energy and thermal resistance to dislocation bypass of obstacles and (ii) reduced rate of strain hardening attributed to reduction of dislocation line tension. These effects are prescribed as a set of first order dependencies of DSS-CP model parameters on H (Castelluccio et al., 2018; Castelluccio and McDowell, 2017). H concentration in lattices and traps are addressed using an existing H transport model (Sofronis and McMeeking, 1989), but framing the coupling in terms of a DSS-CP constitutive model for a single crystal rather than using conventional J_2 elasto-plasticity for polycrystals. A two-way coupling algorithm is implemented in ABAQUS between DSS-CP and H transport models at each time step.

Intensification of blunted crack tip plastic strain is simulated over a full range of H levels, and a parameter sensitivity study is conducted to consider potential ranges of strengths of certain effects. H-enhanced increase of yield strength decreases the localization of plastic strain and the size of the plastic zone ahead of the crack tip. This demonstrates that strengthening cannot explain the H-enhanced localization of crack tip plasticity observed experimentally (Robertson et al., 2015; Sun et al., 1995). In contrast, a reduced rate of strain hardening is observed to lead to significant enhancement of crack tip plasticity, trending towards agreement with the HELP mechanism proposed on the basis of TEM observations. In addition, increased CTODs are predicted in the presence of H, consistent with experiments (Sun et al., 1995). Moreover, it is shown that the two-way coupling algorithm accounts for the effect of increased H-diffusivity on stronger H-effects (i.e., stronger enhancement of crack tip plasticity), consistent with various experimental phenomena.

This work has also demonstrated that in spite of its strong physical basis for directly incorporating dependence of parameters on H, the current DSS-CP model (Castelluccio et al., 2018; Castelluccio and McDowell, 2017) is inadequate to express substantial enhancement of crack tip plastic strain localization that relates to HE processes. We consider that more physical aspects should be introduced in the two-way coupled modeling framework. It is most likely that these salient additional physical processes include.

(1) a more explicit role for coupling of vacancies produced by dislocation plasticity with H trapping and serving as barriers to dislocation motion (Arora et al., 2023; Hatano et al., 2014; Lawrence et al., 2017; Yuan et al., 2023);
(2) influence of H on inhibiting dislocations from undergoing cross-slip, thereby promoting planar slip for common FCC materials (Ferreira et al., 1999; Wen et al., 2004, 2007) and interfaces such as grain boundaries (Hatano et al., 2014; Lawrence et al., 2017);
(3) enhancement of the rate of dislocation generation (Zhu et al., 2008; Zhu et al., 2004) with increasing H concentration;
(4) more sophisticated forms of coupling of H with point and line defects in H diffusion relations;
(5) the slip system level strain rate factor (Kumar and Mahajan, 2020), the H dragging by mobile dislocations (Charles et al., 2022; Dadfarnia et al., 2015; Yuan et al., 2022) and the transient trapping mechanisms (Charles et al., 2021) accounted in the H-transport model. Since the constitutive behavior of the CP model is influenced by loading rate and crystal orientation, the two-way coupled H transport and CP modeling framework developed in this work will potentially serve as a useful tool for studying the micro-mechanisms of crack tip plasticity under different loading rates/orientations;
(6) investigating the effect of H-enhanced intensification or localization of plastic strain on fatigue crack initiation in polycrystals by using micro-mechanism-based/data-driven Fatigue Indicator Parameters (FIPs) (Gu et al., 2020; Stopka et al., 2020) and predict fatigue crack formation lifetime with H (Gu et al., 2023; Guo et al., 2023).

The present work has focused on crack tip strain localization and has not considered mechanisms of damage that serve to reduce resistance to crack extension in HE. With regard to items (3)-(4) above, it is believed that excess H-vacancy clusters and nano-void coalescence contribute in significant ways to HE and further enhance localization of strain beyond those presently accessible to the DSS-CP model (Neeraj et al., 2012).

Recent work by Zirkle et al. (Zirkle et al., 2023) presents such a comprehensive multiscale framework. Vacancies are generated in plastic deformation, with excess vacancy production observed for specimens pre-charged at high H levels (Hatano et al., 2014; Lawrence et al., 2017). These vacancies serve as additional trap sites beyond dislocations and interfaces (Xie et al., 2016). It was shown by that H-stabilized vacancy clusters lead to an increase in barrier resistance to dislocations and H-induced hardening effects within dislocation channels/cells. Excess vacancy accumulation and strain-assisted nano-void coalescence has been observed as a failure pathway associated with the H-enhanced strain-induced vacancy (HESIV) mechanism (Nagumo, 2004), noting high correlation of nano-voids with fracture surfaces at high H concentration (Hatano et al., 2014; Neeraj et al., 2012).

It is worth noting that no single mechanism can completely explain all the associated microstructural aspects that evolve with influence of H (Guo et al., 2024; Neeraj et al., 2012). Rather, we assert that a hierarchy of mechanisms is compiled to confer observed effects of plastic strain localization and reduction of ductility in HE. Recent works have further explored these various aspects of H transport at multiple length and time scales and their influence on their coupling with crystal plasticity modeling (Zirkle et al., 2021a; Zirkle et al., 2021b).

CRediT authorship contribution statement

Tang Gu: Writing – review & editing, Writing – original draft, Visualization, Validation, Software, Methodology, Investigation, Formal analysis, Data curation, Conceptualization. **Baolin Wang:** Software. **Ting Zhu:** Writing – review & editing, Supervision, Project administration, Conceptualization. **Gustavo M. Castelluccio:** Writing – review & editing, Software. **David L. McDowell:** Writing – review & editing, Supervision, Project administration, Funding acquisition, Conceptualization.

Declaration of competing interest

The authors declare that they have no known competing financial interests or personal relationships that could have appeared to influence the work reported in this paper.

Data availability

Data will be made available on request.

Acknowledgments

We acknowledge the financial support of the Fluor Marine Propulsion, LLC. Particularly, we acknowledge the helpful technical discussions with Clint Geller and Ben Anglin (Fluor Marine Propulsion, LLC). Tang Gu thanks Dengke Chen and Yin Zhang (Georgia Institute of Technology) for fruitful discussions, and thanks Jifeng Zhao (QuesTek) for the implementation of H transport model in UMATHT.

Appendix A:. Available experimental data for model validation

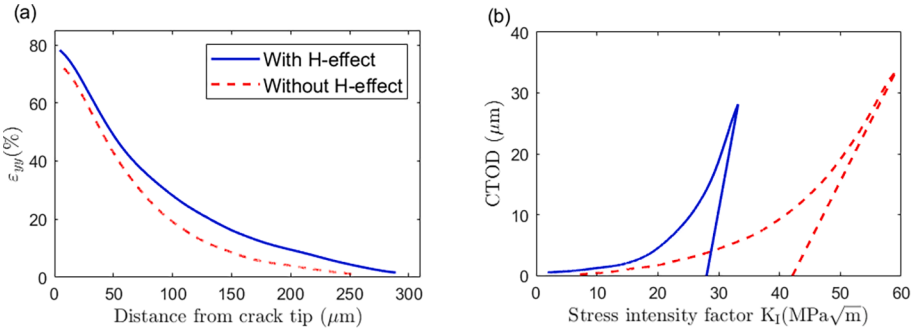

Fig. A15. Available experimental data for the validation of the trend of model prediction (Sun et al., 1995): (a) H-effect on the tensile strain parallel to the crack axis direction (i.e., ε_{yy}) as a function of the radial distance in advance of the crack. The corresponding max stress intensity is $K_I = 35\,\text{MPa}\sqrt{\text{m}}$; (b) CTOD as function of the stress intensity (K_I).

This section summarizes the available experimental data on the strain field near crack tips in single crystal Ni under the influence of H, based on (Sun et al., 1995). Figure A15(a) illustrates the experimental tensile strain parallel to the crack axis direction (i.e., ε_{yy}) as a function of radial distance ahead of the crack, without and with H effects. The H charging methodology by (Abraham and Altstetter, 1995) is similar to that in this work, i.e., involving continuous H charging during crack open to investigate the impact of "external H". The stress intensity factor K_I during loading reaches 35 MPa$\sqrt{\text{m}}$, leading to plastic strains near the crack tip of $\sim$ 70%. The impact of H on effective plastic strain and plastic shear strain (Fig. 8) follows a similar trend to the literature, i.e., H enhances the maximum plastic deformation near the crack tip. Moreover, as shown in Fig. A15(a), it is not evident that H extends the region of plastic deformation significantly, which aligns with the predictive results of this work as well.

Additionally, Sun et al. (Sun et al., 1995) investigated how CTOD varies with stress intensity (K_I) increasing, as summarized in Fig. A15 (b). Their experiment revealed a significant enlargement of CTOD in the presence of H, particularly for stress intensity values ranging from 20 to 30 MPa$\sqrt{\text{m}}$. Conversely, for stress intensity values $K_I \leq 10$ MPa$\sqrt{\text{m}}$, CTOD is only slightly larger with H. These experimental findings align with the predictions in this study, as reported in Table 1, i.e., CTOD increases by $\sim$ 8% under H-charged conditions when the maximum stress intensity is 10 MPa$\sqrt{\text{m}}$. Thus, we conclude that the experimental trends consist well with our simulations for lower stress intensities. For higher stress intensity factors, it may be necessary to further explore more sophisticated forms of DSS-CP constitutive laws along with relations for crack growth to achieve alignment with experimental observations.

Appendix B:. DSS-CP model formulations

In this work, we consider a crystal plasticity model that explicitly describe the effects of mesoscale structures in order to distinguish atomistic scale effects of H from those at larger scale. We continue with the approach we introduced in prior communications (Castelluccio et al., 2018; Castelluccio

and McDowell, 2017) and Section 2 in which the flow rule specifies the shearing rate of up to 12 slip systems in FCC crystals, i.e.,

$$\dot{\gamma}^{\alpha} = \rho_m^s \bar{l} b \nu_G \exp\left(-\frac{\Delta G\left(\tau_{eff}^{\alpha}\right)}{k_B T} \right) \mathrm{sgn}(\tau^{\alpha} - B^{\alpha}). \tag{19}$$

Here, we assume that $\dot{\gamma}^{\alpha}$ has a minimum value as follows greater than $\dot{\gamma}_{th}^{pl} = \frac{b}{\Delta t d_{gr}}$, otherwise $\dot{\gamma}^{\alpha} = 0$ where, Δt is the time increment and d_{gr} is the grain size. The activation enthalpy ΔG pertaining to the mean effective short-range barrier is expressed as

$$\Delta G\left(\tau_{eff}^{\alpha}\right) = F_0 \left(1 - \left[\frac{\tau_{eff}^{\alpha}}{s_t^{0\,\mu}} \right]^p \right)^q. \tag{20}$$

The effective stress that drives the barrier bypass at the slip system level is given by

$$\tau_{eff}^{\alpha} = \langle |\tau^{\alpha} - B^{\alpha}| - S^{\alpha} \rangle. \tag{21}$$

Here, τ^{α} is the local slip system resolved shear stress and S^{α} is the nondirectional athermal threshold stress. In addition, $\langle g \rangle = 0$ if $g \leq 0$, $\langle g \rangle = g$ if $g > 0$. The threshold stress required to bow a dislocation against a dislocation pile-up between dislocation walls is given by

$$S^{\alpha} = S_0^{\alpha} + \alpha_{LE} \frac{\mu b}{(1 - f_w) d_{struct}} + \mu b (A_{ii} \rho^{\alpha})^{1/2} \tag{22}$$

in which S_0^{α} correspond to an intrinsic lattice friction stress, the second term corresponds to the stress required to bow-out a dislocation and depends on the dislocation line energy α_{LE} and dislocation wall volume fraction f_w, and the third term corresponds to the strength interaction between collinear dislocations in pile-ups and depends on the strength of the self-interaction coefficient, A_{ii}. The back stress evolution is based on an Eshelby mean field approach that incorporates dislocation substructure effects (Castelluccio and McDowell, 2017), i.e.,

$$\dot{B}^{\alpha} = \frac{f_w}{1 - f_w} \frac{2\mu(1 - 2S_{1212})}{1 + 4S_{1212}\mu f_{Hill}^S} \dot{\gamma}^{\alpha} \tag{23}$$

Here,

$$S_{1212} = \frac{\pi \left[\eta^2 + (\eta^2 - 1.75 - 2\nu_p \eta^2 + 2\nu_p) C_{12} \right]}{8\pi (1 - \nu_p)(\eta^2 - 1)} \tag{24}$$

$$C_{12} = \frac{2\pi\eta \left(\eta \sqrt{(\eta^2 - 1)} - \cosh^{-1}(\eta) \right)}{\sqrt{(\eta^2 - 1)^3}} \tag{25}$$

$$\nu_p = \frac{\nu + \frac{2}{3}\mu(1 + \nu) f_{Hill}^S}{1 + \frac{4}{3}\mu(1 + \nu) f_{Hill}^S} \tag{26}$$

in which η corresponds to a normalized distance that a dislocation can glide along the dominant slip system relative to the distance between walls. This back stress evolution relation represents the homogenized response of a quasiperiodic dislocation structure that induces residual stress in the material due to the coexistence of a plastically deformable matrix surrounded by an essentially linear elastic structure of dense dislocation walls.

The mean free path for dislocation glide, $\bar{l}$, depends on the local strain range and it is computed following the scheme proposed by (Castelluccio and McDowell, 2017). Thus, the mean advance distance is determined by identifying the appropriate dislocation mesoscale substructures.

$$\bar{l} \approx l_{struct} = \eta d_{struct}. \tag{27}$$

Here, d_{struct} is the characteristic dislocation substructure length scale

$$d_{struct} = \frac{K_{struct} \mu(T) b}{\tau}. \tag{28}$$

(Sauzay and Kubin, 2011) discussed similitude relations and showed that the constant, K_{struct}, ranges from 2 to 4 for a large number of metals and a wide range of cyclic loading conditions. Another characteristic distance associated with the dislocation structure is the wall thickness, which along with the structure spacing and length, determines the wall volume fraction, f_w. A parametrization of f_w based on the maximum plastic shear strain range per cycle among all slip systems is employed

$$f_w = f_{inf} + \left(f_0 - f_{inf} \right) \exp\left(\frac{-\Delta\gamma^{\max}/2}{g_p} \right) \tag{29}$$

where, f_{inf}, f_0, and g_p are material constants that can be estimated by computing f_w from TEM images. The mobile dislocation density on slip system α

results from a balance between dislocation multiplication, annihilation and cross slip

$$\dot{\rho}_m^{s\alpha} = \dot{\rho}_{mult}^{s\alpha} - \dot{\rho}_{annih}^{s\alpha} + \dot{\rho}_{cs}^{s}\Big|^{\zeta\to\alpha} - \dot{\rho}_{cs}^{s}\Big|^{\alpha\to\zeta}. \tag{30}$$

The multiplication rate of mobile screw dislocations for slip system α is computed as

$$\dot{\rho}_{mult}^{s\alpha} = \frac{k_{multi}}{b l_{struct}}|\dot{\gamma}^{\alpha}|. \tag{31}$$

Here $k_{multi}^{cell} = 1$ for cell structures and $k_{multi} = 2$ for parallel walls such as PSBs and labyrinth. The annihilation rate of mobile screw dislocations is given by

$$\dot{\rho}_{annih}^{s\alpha} = \frac{2y_s^{edge}}{b}\rho_m^{s\alpha}|\dot{\gamma}^{\alpha}| - \Upsilon\frac{2\left|\dot{\tau}^{\alpha} - \dot{B}^{\alpha}\right|}{\mu b d_{struct}}\Bigg|^{Unload} \tag{32}$$

where $\Upsilon = 1$ if $\mathrm{sgn}\left(\dot{\tau}^{\alpha} - \dot{B}^{\alpha}\right) \neq \mathrm{sgn}(\tau^{\alpha} - B^{\alpha})$ or $\dot{\gamma}^{\alpha} = 0$; otherwise $\Upsilon = 0$ and $\dot{\rho}_{annih}^{s\alpha}\Big|^{Unload} = 0$. The first term considers the annihilation mechanisms that involve plastic deformation without cross slip (e.g., edge dislocation annihilation), and the second term in Equation (32) represents the annihilation of dislocations due to anelastic deformation upon reversing the local shear stress.

The rate of cross slip of mobile screw dislocations from plane α to $\zeta\left(\dot{\rho}_{cs}^{s}\Big|^{\alpha\to\zeta}\right)$ is estimated using the probabilistic formulation proposed, but considering the local shear stress to account for screening effects from dislocation structures (Castelluccio and McDowell, 2017), i.e.,

$$\dot{\rho}_{cs}^{s\alpha} = -\nu_G\frac{l_{CS}}{d_0}\rho_m^{s\alpha}e^{\left(-V_{CS}\frac{\tau_{III}-|\tau^{\zeta}-B^{\zeta}|}{k_BT}\right)}. \tag{33}$$

Here, ν_G and $l_{CS} \approx d_{struct}$ are the cross slip characteristic frequency and dislocation length, respectively, τ_{III} is the critical cross slip stress, and $|\tau^{\zeta} - B^{\zeta}|$ is the magnitude of the local stress on the cross slip plane of a screw dislocation in system α. The cross-slip activation volume, V_{CS}, depends on the dislocation constraints, and its statistical average has been shown to be inversely proportional to the slip system shear stress, i.e.,

$$V_{CS}^{\alpha} = \frac{V_{CS}^{0}}{|\tau^{\alpha}|} \tag{34}$$

with $v_{CS}^{\alpha} \approx 1000b^3$ MPa. The critical cross slip stress, τ_{III} , which has been estimated between 30 and 80 MPa for Ni, is related to the location of the cyclic shear stress–strain plateau, which is at about 50 MPa. The critical cross slip stress value is computed as

$$\tau_{III} = \frac{\mu b}{4\pi y_s^{screw}} \tag{35}$$

where y_s^{screw} corresponds to the annihilation distance of screw dislocations, which is controlled by the activation energy of cross slip. In summary, the evolution of screw dislocation density is written as

$$\dot{\rho}_m^{s\alpha} = \frac{k_{multi}}{b l_{struct}}|\dot{\gamma}^{\alpha}| - \frac{2y_s^{edge}}{b}\rho_m^{s\alpha}|\dot{\gamma}^{\alpha}| - \frac{2\pi}{\mu b d_{struct}}\left|\dot{\tau}_{eff}\right|\Big|^{Unload} + \nu_G\frac{d_{struct}}{d_0}\left(\phi_{CS}\sum_{\xi=1(\xi\neq\alpha)}^{N}\rho_m^{s\xi}e^{\left(-V_{CS}^{\alpha}\frac{\frac{\mu b}{4\pi y_s^{screw}}-|\tau^{\alpha}-B^{\alpha}|}{k_BT}\right)} - (1-\phi_{CS})\sum_{\xi=1(\xi\neq\alpha)}^{N}\rho_m^{s\alpha}e^{\left(-V_{CS}^{\zeta}\frac{\frac{\mu b}{4\pi y_s^{screw}}-|\tau^{\zeta}-B^{\zeta}|}{k_BT}\right)}\right) \tag{36}$$

Appendix C:. Material parameters and physical constants without H

Previous experimental studies have provided the stress–strain responses of FCC metals and alloys in the presence of interstitial H. For example, (Abraham and Altstetter, 1995) shows responses of polycrystalline FCC 310 SS under monotonic loading at various H concentrations. It was observed unambiguously that the reduction of ductility (i.e., HE) is increasingly significant at higher pre-charged concentrations of H. Also, H-enhanced yield strength increases by as much as a factor of two relative to the case without H. Furthermore, reduction of the rate of strain hardening is observed at extremely high H concentration. Similarly, as shown in Fig. A16(a), H-enhanced yield strength and delay of the onset of Stage II strain hardening response are also observed, for FCC single crystal Ni (Yagodzinskyy et al., 2009). In summary, the H-enhanced yield strength and H-reduced strain hardening rate are commonly observed for FCC metals, and they have been taken into account in our models (see Section 3.2). As illustrated in

Fig. A16(b), Castelluccio and McDowell fitted the DSS-CP parameters to match the monotonic stress–strain curves of FCC Ni at room temperature in the absence of H. In addition, the model responses match well experimental data of single crystal cyclic stress–strain curves of FCC metals (Castelluccio and McDowell, 2017).

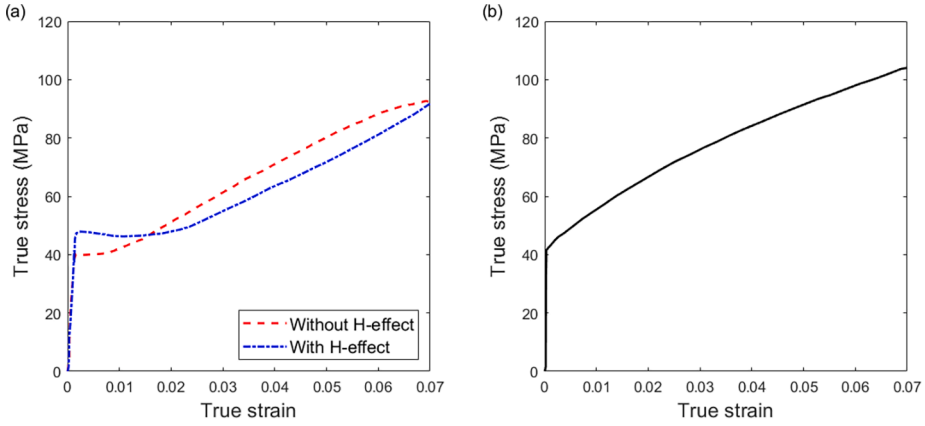

Fig. A16. (a) Monotonic stress-strain curves with and without H charged for single crystal FCC Ni, oriented along [1 6 7] at a strain rate of 9×10^{-5} s^{-1} (Yagodzinskyy et al., 2009). (b) Model responses of DSS-CP without H-effect for single crystal Ni (Castelluccio and McDowell, 2017). Experimental data demonstrates H-enhanced yield strength, as well as H-induced reduction of the strain hardening rate.

This appendix summaries all the material parameters and physical constants without H-effect of DSS-CP model. Table A2 presents the *direct parameters*, which correspond to physical constants associated with the lattice and lattice defect interactions. Since they do not depend on the mesoscopic response of a statistical ensemble, their uncertainty is considered to be relatively low.

Table A2
Direct parameters for FCC Ni.

ν_G	b	C_{11}	C_{12}	C_{44}	C_{44} @0K	μ
10^{12} s^{-1}	2.5×10^{-10} m	249 GPa	155 GPa	114 GPa	127.6 GPa	80.6 GPa

Stochastic parameters are associated with mechanisms or theoretical models that describe the behavior of a statistical ensemble involving dislocations. Table A3 presents the parameters that are amenable to be computed with molecular dynamics. Similarly, Table A4 presents the parameters associated with mesoscale structures, which can be calculated from dislocation dynamics modeling.

Table A3
Parameters related to atomistic mechanisms for FCC Ni.

F_0	s_t^0	p	Q	y_e	y_s	S_0^α	A_{ii}	α_{LE}	V_{CS}^0	ϕ_{CS}
0.985 eV	100 MPa	0.9	1.5	3 nm	13 nm	4 MPa	0.1	1	$1000b^3$	0.5

Table A4
Parameters associated with mesoscale structures for FCC Ni.

η_{cell}	η_{labyr}	η_{PSB}	η_{veins}	K_{struct}	k_{multi}	k_{multi}^{Cell}	f_{inf}	f_0	g_p
1	2	20	50	3.75	2	1	0.24	0.4	1.7

Finally, internal state variables need to be initialized. Table A5 summarizes the initial values implemented.

Table A5
Initial values for internal state values for FCC Ni.

ρ_m^s	d_{struct}	η	η_{veins}	f_w^0	V_{CS}
10^{-10} m^{-2}	10 μm	η_{veins}	50	0.25	$1000b^3$

The material parameters for the H transport model for FCC at room temperature are summarized as follows in Table A6.

Table A6
Material parameters for H transport model for FCC Ni at room temperature.

α_H	β_H	W_B	N_T	V_M	$\overline{V}_H$	D
10	1	10 kJ/mol	Eq. (10)	7.11×10^{-6} m^3/mol	2×10^{-6} m^3/mol	5×10^{-13} m^2/s

Appendix D:. Effect of hydrostatic stress on H distribution

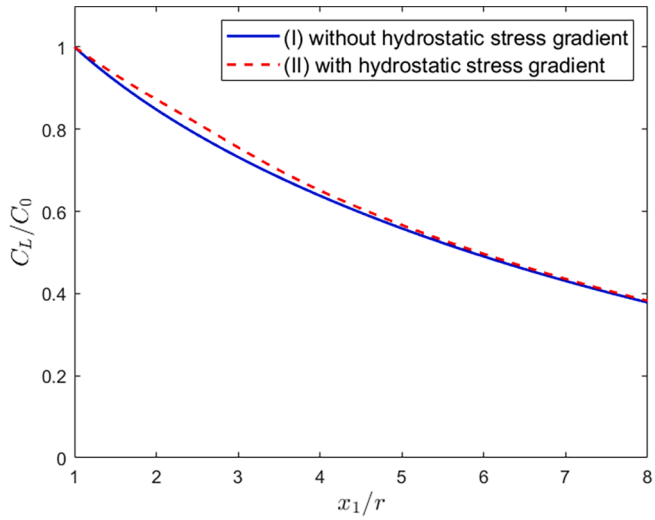

Fig. A17. Normalized H-concentration C_L/C_0 as a function of the normalized distance x_1/r ahead of the crack front. The impact of the hydrostatic stress gradient term in the governing equation for transient H-diffusion is found to be ~ 3 % using the boundary conditions and model parameters established in this study.

Fig. A17 depicts the normalized H-concentration (C_L/C_0) as a function of the normalized distance x_1/r ahead of the crack front. This is for investigating the impact of activating/deactivating the hydrostatic stress gradient term of the governing equation for transient H-diffusion (Eq. (12)). The loading time/magnitude and modeling parameters are kept with prior discussions. The results reveal that, using the parameter adopted in this study, the hydrostatic stress gradient induces an influence of ~ 3% on C_L/C_0, exhibiting more pronounced fluctuations around $x_1/r = \sim 2.5$. We attribute the limited effect of the hydrostatic stress gradient on the H distribution field to factors including (i) the low H-diffusivity of FCC Ni (i.e., 5×10^{-13} m^2/s), (ii) the short H charging duration (51 s), (iii) the small peak loading condition ($K_I = 10$ MPa$\sqrt{m}$). Negligible influence of $\nabla\sigma_H$ on H distribution have also been found in (Martínez-Pañeda et al., 2020) for FCC Ni-Cu superalloy. In Section 5.3, we extended our exploration by assigning an H-diffusivity value of 1.27×10^{-8} m^2/s, akin to BCC materials. This modification shown the peak of C_L/C_0 occurs at approximately $x_1/r = 2$, exceeding 1.05 (see Fig. 13(a)). On the other hand, C_L/C_0 values will always below 1 without accounting for $\nabla\sigma_H$, showing that the impact of $\nabla\sigma_H$ will be more significant for higher H diffusivity.

Appendix E:. Comparison between DSS-CP and J_2 plasticity models

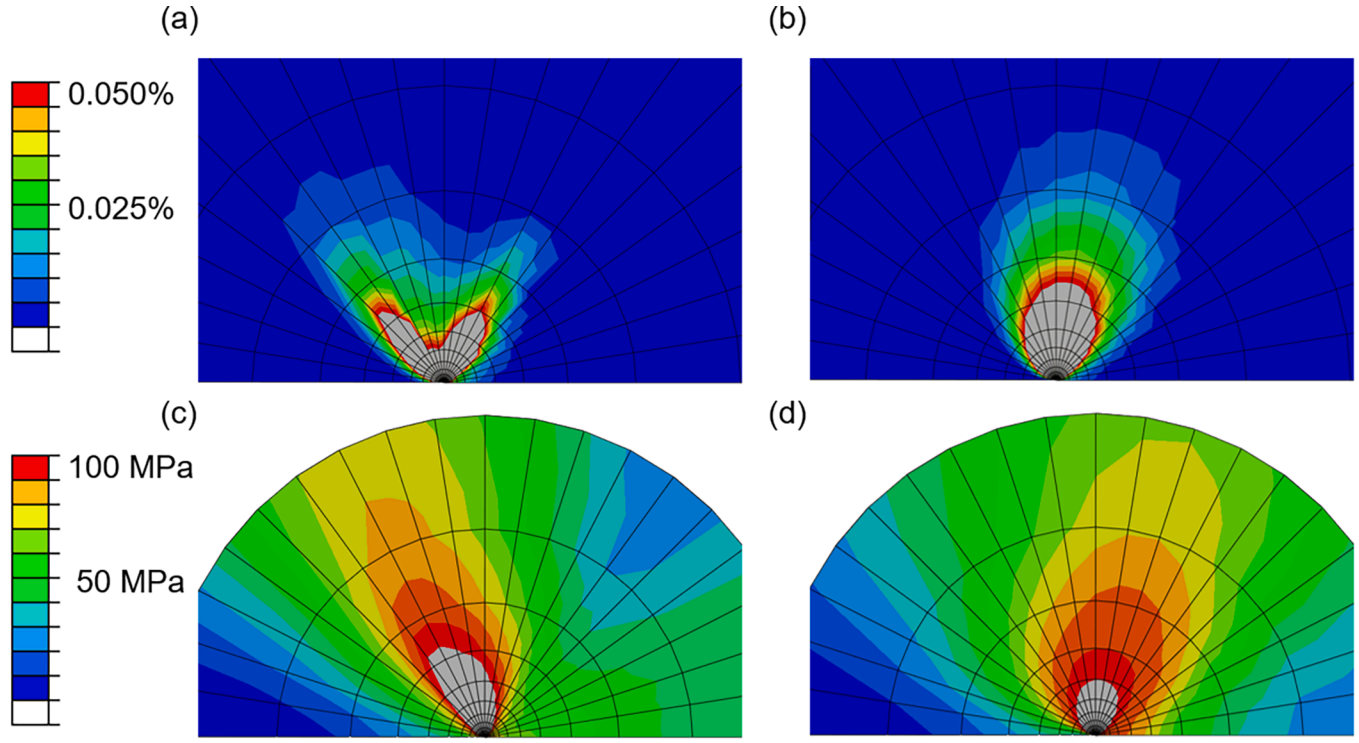

Fig. A18. Comparison between DSS-CP and J_2 plasticity models: (a)-(b) effective plastic strain field obtained by DSS-CP and J_2 plasticity, respectively; (c)-(d) von Mises stress field obtained by DSS-CP and J_2 plasticity, respectively.

In order to verify the crack tip model responses of DSS-CP (without H effect), simulations are carried out by a macroscopic polycrystal phenomenological J_2 plasticity model framework in this Appendix. At first, we calibrate the constitutive relation of Ni using a J_2-based Chaboche model of cyclic plasticity (Smith, 2009), which accounts for both isotropic and kinematic hardening. The adopted parameter combination of J_2 plasticity model matches both monotonic and cyclic stress–strain behavior of polycrystalline Ni. The detailed polycrystalline simulations of DSS-CP has been presented in the previous work (Castelluccio and McDowell, 2017). Note also the experimental yield stress of Ni displays $\sim$ 70 MPa, consistent with our models.

Figure A18(a) and (b) illustrate the crack tip effective plasticity under monotonic uniaxial tensile loading, obtained by DSS-CP and J_2 plasticity models, respectively. Furthermore, Figure A18(c) and (d) show the von Mises stress field by DSS-CP and J_2 plasticity, respectively. The same initial boundary value has been used in Section 4 with $t = 51$ s rise time to a peak loading condition of $K_I = 10\ \mathrm{MPa}\sqrt{\mathrm{m}}$. No H-effect is taken into account for these crack tip simulations. It is found that these two models display a similar size of plastic zone and von Mises stress field ahead of crack tip, demonstrating that the crack tip model responses of DSS-CP model are reasonable. As expected, the contours of mechanical fields determined by DSS-CP model reflect the underlying anisotropic character in the case of a single crystal (i.e., Figure A18(a) and (c)).

References

Abraham, D.P., Altstetter, C.J., 1995. The effect of hydrogen on the yield and flow stress of an austenitic stainless steel. Metall. Mater. Trans. A 26, 2849–2858.

Angelo, J.E., Moody, N.R., Baskes, M.I., 1995. Trapping of hydrogen to lattice defects in nickel. Model. Simul. Mater. Sci. Eng. 3, 289–307.

Arora, A., Singh, H., Adlakha, I., Mahajan, D.K., 2023. On the role of vacancy-hydrogen complexes on dislocation nucleation and propagation in metals. Model. Simul. Mater. Sci. Eng. 31, 085006.

Aubert, I., Olive, J.-M., Saintier, N., 2010. The effect of internal hydrogen on surface slip localisation on polycrystalline AISI 316L stainless steel. Mater. Sci. Eng. A 527, 5858–5866.

Baskes, M., Sha, X., Angelo, J., Moody, N., 1997. Trapping of hydrogen to lattice defects in nickel. Model. Simul. Mater. Sci. Eng. 5, 651.

Bichon, B.J., Eldred, M.S., Swiler, L.P., Mahadevan, S., McFarland, J.M., 2008. Efficient global reliability analysis for nonlinear implicit performance functions. AIAA J. 46, 2459–2468.

Boyer, H.E., Gall, T.L., 1985. Metals handbook; desk edition.

Castelluccio, G.M., Geller, C.B., McDowell, D.L., 2018. A rationale for modeling hydrogen effects on plastic deformation across scales in FCC metals. Int. J. Plast 111, 72–84.

Castelluccio, G.M., McDowell, D.L., 2017. Mesoscale cyclic crystal plasticity with dislocation substructures. Int. J. Plast 98, 1–26.

Charles, Y., Nguyen, H.T., Gaspérini, M., 2017. Comparison of hydrogen transport through pre-deformed synthetic polycrystals and homogeneous samples by finite element analysis. Int. J. Hydrogen Energy 42, 20336–20350.

Charles, Y., Mougenot, J., Gaspérini, M., 2021. Effect of transient trapping on hydrogen transport near a blunting crack tip. Int. J. Hydrogen Energy 46, 10995–11003.

Charles, Y., Mougenot, J., Gasperini, M., 2022. Modeling hydrogen dragging by mobile dislocations in finite element simulations. Int. J. Hydrogen Energy 47, 13746–13761.

Chen, D., Costello, L.L., Geller, C.B., Zhu, T., McDowell, D.L., 2019. Atomistic modeling of dislocation cross-slip in nickel using free-end nudged elastic band method. Acta 168, 436–447.

Cuitino, A.M., Ortiz, M., 1993. Computational modelling of single crystals. Model. Simul. Mater. Sci. Eng. 1, 225–263.

Dadfarnia, M., Martin, M.L., Nagao, A., Sofronis, P., Robertson, I.M., 2015. Modeling hydrogen transport by dislocations. J. Mech. Phys. Solids 78, 511–525.

Depraetere, R., De Waele, W., Hertelé, S., 2021. Fully-coupled continuum damage model for simulation of plasticity dominated hydrogen embrittlement mechanisms. Comput. Mater. Sci 200, 110857.

Fekete, B., Ai, J., Yang, J., Han, J., Maeng, W., Macdonald, D.D., 2018. An advanced coupled environment fracture model for hydrogen-induced cracking in alloy 600 in PWR primary heat transport environment. Theor. Appl. Fract. Mech. 95, 233–241.

Feng, Z., Li, X., Song, X., Gu, T., Zhang, Y., 2022. Hydrogen embrittlement of CoCrFeMnNi high-entropy alloy compared with 304 and IN718 alloys. Metals 12, 998.

Ferreira, P., Robertson, I., Birnbaum, H., 1999. Hydrogen effects on the character of dislocations in high-purity aluminum. Acta Mater. 47, 2991–2998.

Ghermaoui, I., Oudriss, A., Metsue, A., Milet, R., Madani, K., Feaugas, X., 2019. Multiscale analysis of hydrogen-induced softening in fcc nickel single crystals oriented for multiple-slips: elastic screening effect. Sci. Rep. 9, 13042.

Gobbi, G., Colombo, C., Miccoli, S., Vergani, L., 2019. A fully coupled implementation of hydrogen embrittlement in FE analysis. Adv. Eng. Softw. 135, 102673.

Gu, T., Castelnau, O., Forest, S., Hervé-Luanco, E., Lecouturier, F., Proudhon, H., Thilly, L., 2017. Multiscale modeling of the elastic behavior of architectured and nanostructured Cu–Nb composite wires. Int. J. Solids Struct. 121, 148–162.

Gu, T., Medy, J.-R., Klosek, V., Castelnau, O., Forest, S., Herve-Luanco, E., Lecouturier-Dupouy, F., Proudhon, H., Renault, P.-O., Thilly, L., 2019. Multiscale modeling of the elasto-plastic behavior of architectured and nanostructured Cu-Nb composite wires and comparison with neutron diffraction experiments. Int. J. Plast 122, 1–30.

Gu, T., Stopka, K.S., Xu, C., McDowell, D.L., 2020. Prediction of maximum fatigue indicator parameters for duplex Ti–6Al–4V using extreme value theory. Acta Mater. 188, 504–516.

Gu, T., Stopka, K.S., Xu, C., McDowell, D.L., 2023. Modeling the statistical distribution of fatigue crack formation lifetime in large volumes of polycrystalline microstructures. Acta Mater. 247, 118715.

Guo, C., Liu, S., Gu, T., Zhou, L., Zhao, D., Dong, L., Zhang, Q., Wang, Q., Ling, C., 2024. Coupled effects of hydrogen embrittlement and temperature and surface roughness on the mechanical properties of GS80A steel. Eng. Failure Anal. 160, 108112.

Guo, C., Liu, S., Zou, Y., Zhao, D., Cheng, M., Gu, T., Liu, Y., Zhang, Q., Wang, Q., Feng, Z., 2023. Fatigue Properties and Life Prediction of GS80A Steel Under the Effect of Hydrogen-Rich Environment. JOM 75, 1306–1318.

Hachet, G., Oudriss, A., Barnoush, A., Milet, R., Wan, D., Metsue, A., Feaugas, X., 2020. The influence of hydrogen on cyclic plasticity of <001> oriented nickel single crystal. Part I: Dislocation organisations and internal stresses. Int. J. Plasticity 126, 102611.

Hachet, G., Oudriss, A., Barnoush, A., Hajilou, T., Wang, D., Metsue, A., Feaugas, X., 2021. Antagonist softening and hardening effects of hydrogen investigated using nanoindentation on cyclically pre-strained nickel single crystal. Mater. Sci. Eng. A 803, 140480.

Han, G., He, J., Fukuyama, S., Yokogawa, K., 1998. Effect of strain-induced martensite on hydrogen environment embrittlement of sensitized austenitic stainless steels at low temperatures. Acta Mater. 46, 4559–4570.

Hatano, M., Fujinami, M., Arai, K., Fujii, H., Nagumo, M., 2014. Hydrogen embrittlement of austenitic stainless steels revealed by deformation microstructures and strain-induced creation of vacancies. Acta Mater. 67, 342–353.

Ilin, D.N., Saintier, N., Olive, J.-M., Abgrall, R., Aubert, I., 2014. Simulation of hydrogen diffusion affected by stress-strain heterogeneity in polycrystalline stainless steel. Int. J. Hydrogen Energy 39, 2418–2422.

Kocks, U., Mecking, H., 2003. Physics and phenomenology of strain hardening: the FCC case. Prog. Mater Sci. 48, 171–273.

Koric, S., Hibbeler, L.C., Thomas, B.G., 2009. Explicit coupled thermo-mechanical finite element model of steel solidification. Int. J. Numer. Meth. Eng. 78, 1–31.

Krom, A.H., Koers, R.W., Bakker, A., 1999. Hydrogen transport near a blunting crack tip. J. Mech. Phys. Solids 47, 971–992.

Kumar, R., Mahajan, D.K., 2020. Hydrogen distribution in metallic polycrystals with deformation. J. Mech. Phys. Solids 135, 103776.

Lawrence, S.K., Yagodzinskyy, Y., Hänninen, H., Korhonen, E., Tuomisto, F., Harris, Z.D., Somerday, B.P., 2017. Effects of grain size and deformation temperature on hydrogen-enhanced vacancy formation in Ni alloys. Acta Mater. 128, 218–226.

Li, K., Tang, B., Zhang, M., Zhao, L., Liu, X., Fan, J., Li, J., 2023a. A hydrogen diffusion model considering grain boundary characters based on crystal plasticity framework. Int. J. Plast 169, 103740.

Li, X., Wang, C., Feng, H., Gu, T., Zhang, J., Zhang, Y., Ren, X., 2023b. Simultaneously enhancing strength and hydrogen embrittlement resistance of pure iron via gradient microstructure. Corros. Sci. 218, 111134.

Lin, P., Vivekanandan, V., Anglin, B., Geller, C., El-Azab, A., 2021a. Incorporating point defect generation due to jog formation into the vector density-based continuum dislocation dynamics approach. J. Mech. Phys. Solids 156, 104609.

Lin, P., Vivekanandan, V., Starkey, K., Anglin, B., Geller, C., El-Azab, A., 2021b. On the computational solution of vector-density based continuum dislocation dynamics models: A comparison of two plastic distortion and stress update algorithms. Int. J. Plast 138, 102943.

Luo, H., Li, Z., Raabe, D., 2017. Hydrogen enhances strength and ductility of an equiatomic high-entropy alloy. Sci. Rep. 7, 9892.

Martínez-Pañeda, E., Golahmar, A., Niordson, C.F., 2018. A phase field formulation for hydrogen assisted cracking. Comput. Methods Appl. Mech. Eng. 342, 742–761.

Martínez-Pañeda, E., Harris, Z.D., Fuentes-Alonso, S., Scully, J.R., Burns, J.T., 2020. On the suitability of slow strain rate tensile testing for assessing hydrogen embrittlement susceptibility. Corros. Sci. 163, 108291.

Moody, N., Robinson, S., Garrison Jr, W., 1990. Hydrogen effects on the properties and fracture modes of iron-based alloys. Res Mech. 30, 143–206.

Murakami, Y., Kanezaki, T., Mine, Y., Matsuoka, S., 2008. Hydrogen embrittlement mechanism in fatigue of austenitic stainless steels. Metall. Mater. Trans. A 39, 1327–1339.

Nagumo, M., 2004. Hydrogen related failure of steels–a new aspect. Mater. Sci. Technol. 20, 940–950.

Neeraj, T., Srinivasan, R., Li, J., 2012. Hydrogen embrittlement of ferritic steels: observations on deformation microstructure, nanoscale dimples and failure by nanovoiding. Acta Mater. 60, 5160–5171.

Ogosi, E., Siddiq, A., Asim, U.B., Kartal, M.E., 2020. Crystal plasticity based study to understand the interaction of hydrogen, defects and loading in austenitic stainless-steel single crystals. Int. J. Hydrogen Energy 45, 32632–32647.

Oh, C.-S., Kim, Y.-J., Yoon, K.-B., 2010. Coupled analysis of hydrogen transport using ABAQUS. Journal of Solid Mechanics and Materials Engineering 4, 908–917.
Oriani, R.A., 1970. The diffusion and trapping of hydrogen in steel. Acta Metall. 18, 147–157.
Patil, S.D., Narasimhan, R., Biswas, P., Mishra, R., 2008a. Crack tip fields in a single edge notched aluminum single crystal specimen. J. Eng. Mater. Technol. 130.
Patil, S.D., Narasimhan, R., Mishra, R., 2008b. A numerical study of crack tip constraint in ductile single crystals. J. Mech. Phys. Solids 56, 2265–2286.
Rice, J.R., 1987. Tensile crack tip fields in elastic-ideally plastic crystals. Mech. Mater. 6, 317–335.
Robertson, I.M., Sofronis, P., Nagao, A., Martin, M., Wang, S., Gross, D., Nygren, K., 2015. Hydrogen embrittlement understood. Metall. Mater. Trans. B 46, 1085–1103.
Saeedvafa, M., Rice, J.R., 1989. Crack tip singular fields in ductile crystals with taylor power-law hardening: II: Plane strain. J. Mech. Phys. Solids 37, 673–691.
Saintier, N., Awane, T., Olive, J.-M., Matsuoka, S., Murakami, Y., 2011. Analyses of hydrogen distribution around fatigue crack on type 304 stainless steel using secondary ion mass spectrometry. Int. J. Hydrogen Energy 36, 8630–8640.
Sauzay, M., Kubin, L.P., 2011. Scaling laws for dislocation microstructures in monotonic and cyclic deformation of fcc metals. Prog. Mater Sci. 56, 725–784.
Schebler, G.J., 2011. On the mechanics of the hydrogen interaction with single crystal plasticity. University of Illinois. Urbana-Champaign.
Schuster, G., Altstetter, C., 1983. Fatigue of stainless steel in hydrogen. Metall. Trans. A 14, 2085–2090.
Singh, V., Kumar, R., Charles, Y., Mahajan, D.K., 2022. Coupled diffusion-mechanics framework for simulating hydrogen assisted deformation and failure behavior of metals. Int. J. Plast 157, 103392.
Smith, M., 2009. ABAQUS/Standard User's Manual, Version 6.9. Dassault Systemes Simulia Corp.
Sofronis, P., McMeeking, R.M., 1989. Numerical analysis of hydrogen transport near a blunting crack tip. J. Mech. Phys. Solids 37, 317–350.
Stopka, K.S., Gu, T., McDowell, D.L., 2020. Effects of algorithmic simulation parameters on the prediction of extreme value fatigue indicator parameters in duplex Ti-6Al-4V. Int. J. Fatigue 141, 105865.
Sun, S., Shiozawa, K., Gu, J., Chen, N., 1995. Investigation of deformation field and hydrogen partition around crack tip in fcc single crystal. Metall. Mater. Trans. A 26, 731–739.
Tehranchi, A., Zhou, X., Curtin, W., 2020. A decohesion pathway for hydrogen embrittlement in nickel: Mechanism and quantitative prediction. Acta Mater. 185, 98–109.
Thomas, G., 1980. Hydrogen trapping in FCC metals. Sandia National Labs, Livermore, CA (USA).
Tien, J., Thompson, A.W., Bernstein, I., Richards, R.J., 1976. Hydrogen transport by dislocations. Metall. Trans. A 7, 821–829.
Vasios, N., 2015. Crystal plasticity: A rate-independent constitutive model, the effect of hydrogen concentration, Diploma Thesis, University of Thessaly, Greece.
Völkl, J., Alefeld, G., 1978. Diffusion of hydrogen in metals. Hydrogen in Metals I, 321–348.
Wang, S., Nagao, A., Edalati, K., Horita, Z., Robertson, I.M., 2017. Influence of hydrogen on dislocation self-organization in Ni. Acta Mater. 135, 96–102.
Wang, S., Nagao, A., Sofronis, P., Robertson, I.M., 2018. Hydrogen-modified dislocation structures in a cyclically deformed ferritic-pearlitic low carbon steel. Acta Mater. 144, 164–176.
Wen, M., Fukuyama, S., Yokogawa, K., 2004. Hydrogen-affected cross-slip process in fcc nickel. Phys. Rev. B 69, 174108.
Wen, M., Fukuyama, S., Yokogawa, K., 2007. Cross-slip process in fcc nickel with hydrogen in a stacking fault: An atomistic study using the embedded-atom method. Phys. Rev. B 75, 144110.
Xie, D., Li, S., Li, M., Wang, Z., Gumbsch, P., Sun, J., Ma, E., Li, J., Shan, Z., 2016. Hydrogenated vacancies lock dislocations in aluminium. Nat. Commun. 7, 1–7.
Yagodzinskyy, Y., Saukkonen, T., Hänninen, H., Tuomisto, F., Barannikova, S., Zuev, L., 2009. Effect of hydrogen on plastic strain localization in single crystals of nickel and austenitic stainless steel, Proceedings of the 2008 International Hydrogen Conference, pp. 97-104.
Yu, H., Cocks, A.C., Tarleton, E., 2020. Simulating hydrogen in fcc materials with discrete dislocation plasticity. Int. J. Hydrogen Energy 45, 14565–14577.
Yuan, S., Zhu, Y., Huang, M., Liang, S., Li, Z., 2020. Dislocation-density based crystal plasticity model with hydrogen-enhanced localized plasticity in polycrystalline face-centered cubic metals. Mech. Mater. 148, 103472.
Yuan, S., Zhu, Y., Zhao, L., Liang, S., Huang, M., Li, Z., 2022. Key role of plastic strain gradient in hydrogen transport in polycrystalline materials. Int. J. Plast 158, 103409.
Yuan, S., Zhu, Y., Huang, M., Zhao, L., Liang, S., Li, Z., 2023. A coupled diffusional-mechanical model accounting for hydrogen enhancements of strain-induced dislocations and vacancies. Mech. Mater. 186, 104781.
Zhu, T., Li, J., Samanta, A., Kim, H.G., Suresh, S., 2007. Interfacial plasticity governs strain rate sensitivity and ductility in nanostructured metals. Proceedings of the National Academy of Sciences of the USA 104, 3031–3036.
Zhu, T., Li, J., Yip, S., 2004. Atomistic study of dislocation loop emission from a crack tip. Phys. Rev. Lett. 93, 025503.
Zhu, T., Li, J., Samanta, A., Leach, A., Gall, K., 2008. Temperature and strain-rate dependence of surface dislocation nucleation. Phys. Rev. Lett. 100, 025502.
Zirkle, T., Costello, L., McDowell, D.L., 2021a. Crystal plasticity modeling of hydrogen and hydrogen-related defects in initial yield and plastic flow of single-crystal stainless steel 316L. Metall. Mater. Trans. A 52, 3961–3977.
Zirkle, T., Costello, L., Zhu, T., McDowell, D.L., 2021b. Modeling Dislocation-Mediated Hydrogen Transport and Trapping in Face-Centered Cubic Metals. J. Eng. Mater. Technol. 144, 011005.
Zirkle, T., Zhu, T., McDowell, D.L., 2023. Multiscale Modeling of Hydrogen-Affected Crack Tip Damage using a Fully Coupled Chemomechanical Crystal Plasticity Framework for Austenitic Stainless Steel. Int. J. Multiscale Comput. Eng. 21, 21–65.